

2

AD-A231 792

SSS-TR-90-11550

GL-TR-90-0189

**A SIMPLE PHYSICAL MODEL FOR SPALL FROM NUCLEAR
EXPLOSIONS BASED UPON TWO-DIMENSIONAL NONLINEAR
NUMERICAL SIMULATIONS**

T.G. Barker
S.M. Day

Maxwell Laboratories, Inc.
S-CUBED Division
P.O. Box 1620
La Jolla, CA 92038-1620

DTIC
ELECTE
FEB 06 1991
S D D

May 1990

Scientific Report No. 3

Approved for Public Release; Distribution Unlimited

Geophysics Laboratory
Air Force Systems Command
United States Air Force
Hanscom Air Force Base, MA 01731-5000


91 2 05 066

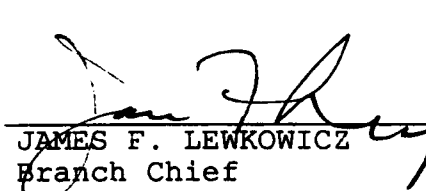
SPONSORED BY
Defense Advanced Research Projects Agency
Nuclear Monitoring Research Office
ARPA ORDER NO 5307

MONITORED BY
Geophysics Laboratory
F19628-89-C-0043

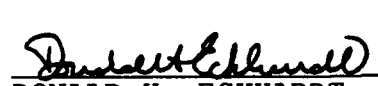
The views and conclusions contained in this document are those of the authors and should not be interpreted as representing the official policies, either expressed or implied, of the Defense Advanced Research Projects Agency or the U.S. Government.

This technical report has been reviewed and is approved for publication.


JAMES F. LEWKOWICZ
Contract Manager
Solid Earth Geophysics Branch
Earth Sciences Division


JAMES F. LEWKOWICZ
Branch Chief
Solid Earth Geophysics Branch
Earth Sciences Division

FOR THE COMMANDER


DONALD H. ECKHARDT, Director
Earth Sciences Division

This report has been reviewed by the ESD Public Affairs Office (PA) and is releasable to the National Technical Information Service (NTIS).

Qualified requestors may obtain additional copies from the Defense Technical Information Center. All others should apply to the National Technical Information Service.

If your address has changed, or if you wish to be removed from the mailing list, or if the addressee is no longer employed by your organization, please notify GL/IMA, Hanscom AFB, MA 01731-5000. This will assist us in maintaining a current mailing list.

Do not return copies of this report unless contractual obligations or notices on a specific document requires that it be returned.

REPORT DOCUMENTATION PAGE			Form Approved OMB No. 0704-0188	
<small>Public reporting burden for this collection of information is estimated to average 1 hour per response, including the time for reviewing instructions, searching existing data sources, gathering and maintaining the data needed, and completing and reviewing the collection of information. Send comments regarding this burden estimate or any other aspect of this collection of information, including suggestions for reducing this burden, to Washington Headquarters Services, Directorate for Information Operations and Reports, 1215 Jefferson Davis Highway, Suite 1204, Arlington VA 22202-4302, and to the Office of Management and Budget, Paperwork Reduction Project (0704-0188), Washington, DC 20503</small>				
1. AGENCY USE ONLY (Leave blank)		2. REPORT DATE May 1990		3. REPORT TYPE AND DATES COVERED Scientific Report No. 3
4. TITLE AND SUBTITLE A SIMPLE PHYSICAL MODEL FOR SPALL FROM NUCLEAR EXPLOSIONS BASED UPON TWO-DIMENSIONAL NONLINEAR NUMERICAL SIMULATIONS			5. FUNDING NUMBERS PE 62714E PR9AIO TA OA WU BG Contract F19628-89-C-0043	
6. AUTHOR(S) Barker, T. G. and Day, S. M.				
7. PERFORMING ORGANIZATION NAME(S) AND ADDRESS(ES) Maxwell Laboratories, Inc. S-CUBED Division P.O. Box 1620 La Jolla, CA 92038-1620			8. PERFORMING ORGANIZATION REPORT NUMBER SSS-TR-90-11550	
9. SPONSORING/MONITORING AGENCY NAME(S) AND ADDRESS(ES) Geophysics Laboratory Hanscom Air Force Base, MA 01731-5000 Contract Manager: James Lewkowicz/LWH			10. SPONSORING/MONITORING AGENCY REPORT NUMBER GL-TR-90-0189	
11. SUPPLEMENTARY NOTES				
12a. DISTRIBUTION/AVAILABILITY STATEMENT Approved for public release; distribution unlimited.			12b. DISTRIBUTION CODE	
13. ABSTRACT (Maximum 200 words) <p>We examine the effect of spall on the source function for explosion waveforms using two-dimensional nonlinear numerical simulations of explosions. A simple, physical model for spall is developed by comparing the complete two-dimensional waveform with the waveform generated by a one-dimensional explosion plus a shallow tension crack in the same layered medium. This is an extension to higher frequencies of the spall model derived by Day, <i>et al.</i> (1983). The tension crack is parameterized by its radius, depth and a distribution of takeoff velocities over its surface.</p> <p>P-waves generated by the two-dimensional simulation are modeled very well by the simple tension crack plus explosion model, and the resulting parameters for the spall model are consistent with the limited set of near-field observations of spall. The model underestimates the shear waves generated in the two-dimensional calculations, indicating that the source of shear waves is more complex than the simple explosion plus tension crack model. P-waves generated by the tension are found to have a narrowband spectrum proportional to $\omega^{-5/2}$ at high frequencies, with a peak typically in the frequency range between 0.5 and 5 Hz, which puts it in the middle of the frequency range where short period magnitudes are commonly measured.</p>				
14. SUBJECT TERMS Nuclear Explosions Spall Finite Difference Calculations Seismic Waves			15. NUMBER OF PAGES 82	
			16. PRICE CODE	
17. SECURITY CLASSIFICATION OF REPORT UNCLASSIFIED	18. SECURITY CLASSIFICATION OF THIS PAGE UNCLASSIFIED	19. SECURITY CLASSIFICATION OF ABSTRACT UNCLASSIFIED	20. LIMITATION OF ABSTRACT SAR	

TABLE OF CONTENTS

SECTION		PAGE
1	INTRODUCTION	1
2	THEORY	3
3	COMPARISONS WITH NUMERICAL SIMULATIONS	21
4	SUMMARY AND CONCLUSIONS	60

Accession For	
NTIS CRA&I	✓
DTIC TAB	[]
Unannounced	[]
Justification	
By	
Distribution	
Availability Codes	
Dist	Availability Codes
A-1	



LIST OF ILLUSTRATIONS

FIGURE		PAGE
1	The tension crack model for spall from an explosion.	4
2	Geometry for a tension crack in a layered medium.	6
3	Schematic drawing of the detachment acceleration history which is proportional to the far-field P-wave displacement time history.	18
4	Schematic drawing of the far-field P-wave displacement spectrum.	20
5	Sketch of the P waves from the 2D nonlinear simulations (left) and 1D cases (right) in which an RDP (from a 1D nonlinear simulation) is embedded in an elastic medium.	22
6	Comparison of the far-field P-waves from the 1D (solid lines) and 2D (dashed lines) Shagan River simulations for four depths of burial at a take-off angle of 10° .	24
7	Comparison of the far-field P-waves from the 1D (solid lines) and 2D (dashed lines) Shagan River simulations for four depths of burial at a take-off angle of 20° .	25
8	Comparison of the far-field P-waves from the 1D (solid lines) and 2D (dashed lines) Shagan River simulations for four depths of burial at a take-off angle of 30° .	26
9	Comparison of the far-field SV-waves from the 1D (solid lines) and 2D (dashed lines) Shagan River simulations for four depths of burial at a take-off angle of 10° .	27
10	Comparison of the far-field SV-waves from the 1D (solid lines) and 2D (dashed lines) Shagan River simulations for four depths of burial at a take-off angle of 20° .	28

11	Comparison of the far-field SV-waves from the 1D (solid lines) and 2D (dashed lines) Shagan River simulations for four depths of burial at a take-off angle of 30° .	29
12	Comparison of the far-field P-waves from the 2D-1D (solid lines) Shagan River simulations with the tension crack model (dashed lines) at three take-off angles for a depth of burial of 200 m.	32
13	Comparison of the far-field P-waves from the 2D-1D (solid lines) Shagan River simulations with the tension crack model (dashed lines) at three take-off angles for a depth of burial of 300 m.	33
14	Comparison of the far-field P-waves from the 2D-1D (solid lines) Shagan River simulations with the tension crack model (dashed lines) at three take-off angles for a depth of burial of 680 m.	34
15	Comparison of the far-field P-waves from the 2D-1D (solid lines) Shagan River simulations with the tension crack model (dashed lines) at three take-off angles for a depth of burial of 980 m.	35
16	Comparison of the far-field SV-waves from the 2D-1D (solid lines) Shagan River simulations with the tension crack model (dashed lines) at three take-off angles for a depth of burial of 200 m.	37
17	Comparison of the far-field SV-waves from the 2D-1D (solid lines) Shagan River simulations with the tension crack model (dashed lines) at three take-off angles for a depth of burial of 300 m.	38
18	Comparison of the far-field SV-waves from the 2D-1D (solid lines) Shagan River simulations with the tension crack model (dashed lines) at three take-off angles for a depth of burial of 680 m.	39
19	Comparison of the far-field SV-waves from the 2D-1D (solid lines) Shagan River simulations with the tension crack model (dashed lines) at three take-off angles for a depth of burial of 980 m.	40

20	Sketch of alternative sources of SV: the compensated linear vector dipole (left) and a distributed double-couple (right).	41
21	Comparison of the far-field SV-waves from the 2D-1D (solid lines) Shagan River simulations with the CLVD model (dashed lines) (with no tension crack contribution) at three take-off angles for a depth of burial of 980 m.	43
22	Comparison of the far-field P-waves from the 2D-1D (solid lines) Shagan River simulations with the CLVD model (dashed lines) (with no tension crack contribution) at three take-off angles for a depth of burial of 980 m.	44
23	Comparison of 2D-1D far-field SV-waves (solid lines) and results using 1/2 CLVD and 1/2 tension crack contributions (dashed lines) at three take-off angles for a depth of burial of 680 m from the Shagan River simulations.	46
24	Comparison of 2D-1D far-field P-waves (solid lines) and results using 1/2 CLVD and 1/2 tension crack contributions (dashed lines) at three take-off angles for a depth of burial of 680 m from the Shagan River simulations.	47
25	Comparison of the far-field P-waves from the 1D (solid lines) and 2D (dashed lines) Pahute Mesa simulations for three depths of burial at a take-off angle of 3.3° .	49
26	Comparison of the far-field P-waves from the 1D (solid lines) and 2D (dashed lines) Pahute Mesa simulations for three depths of burial at a take-off angle of 11.4° .	50
27	Comparison of the far-field P-waves from the 1D (solid lines) and 2D (dashed lines) Pahute Mesa simulations for three depths of burial at a take-off angle of 16.7° .	51
28	Comparison of the far-field P-waves from the 2D-1D (solid lines) Pahute Mesa simulations with the tension crack model (dashed lines) at three take-off angles for a depth of burial of 200 m.	52

29	Comparison of the far-field P-waves from the 2D-1D (solid lines) Pahute Mesa simulations with the tension crack model (dashed lines) at three take-off angles for a depth of burial of 680 m.	53
30	Comparison of the far-field P-waves from the 2D-1D (solid lines) Pahute Mesa simulations with the tension crack model (dashed lines) at three take-off angles for a depth of burial of 980 m.	54
31	Comparison of the far-field P-waves from the 2D-1D (solid lines) Pahute Mesa simulations with the tension crack model with constant crack opening (dashed lines) at three take-off angles for a depth of burial of 980 m.	56
32	Comparison of the far-field SV-waves from the 2D-1D (solid lines) Pahute Mesa simulations with the tension crack model with Gaussian slip distribution (dashed lines) at three take-off angles for a depth of burial of 680 m.	58

1. INTRODUCTION

Several models have been proposed for the spall process that accompanies most nuclear explosions. The models are very difficult to validate directly because (1) the features of the process that can be measured, such as vertical motion at the surface, are observed at only a few locations above the shot, and (2) there are few observations of features such as the depth and area of the spall zone and the distribution of motions within the zone. Two-dimensional nonlinear simulations of the explosion, which include the physics of the free-surface interactions, provide an opportunity to examine spall, and to find simple models to represent it. We present a linear model for the spall process and find its parameters by comparing with the seismic waves from explosion simulations.

Using a form of the elastodynamic representation theorem, we have calculated the short-period body waves emanating from the source zone of the numerical simulations. The implications for teleseismic magnitude measurements were discussed in Day, *et al.* (1986) and McLaughlin, *et al.* (1988). By comparing these P and SV wavefields with one-dimensional nonlinear calculations (which do not include the nonlinear effects of the free-surface), we can isolate that part of the wave field due to the nonlinear interaction with the free-surface. We find that a simple tension crack with an opening that propagates with the pP arrival from the explosion fits P-waves from simulations of both Pahute Mesa and Shagan River tests. However, the model which fits the P-wave radiation generates SV-waves that are too small, which indicates that there are additional sources of shear waves in the finite difference simulations.

The tension crack model, proposed in its original form by Day, *et al.* (1983), is a physical model whose parameters can be compared directly to field observations. The parameters of the model are spall depth and area, detachment velocity, and momentum. The parameters inferred from the simulations are consistent with published estimates of these values. The time dependence of the far-field waveforms is a natural consequence of the model and requires no *ad hoc* choice of time history to include the effects of source finiteness, the importance of which has been pointed out by Stump (1985). Although there is a trade-off between the parameters of the model, the amplitudes and waveforms from the two-dimensional (2D) simulations tightly constrain the set of parameters which fit the simulations.

The form for the linear source representation of the spall model is such that it can easily be added to a one-dimensional (1D) explosion source to compute regional and teleseismic synthetic seismograms. In a companion paper, McLaughlin, *et al.* (1990), use the model to compute the effects of spall on synthetic regional explosion seismograms. It is found that the spall contribution to the Lg signal is comparable to the direct explosion contribution.

In the following, we describe the tension crack model and show how it has been implemented. We then compare the body waves from the model with those from the numerical simulations and compare the parameters of the model with field observations. Our conclusions are presented in the last section.

2. THEORY

2.1. Tension Crack in a Layered Medium

Our model for the spall process is a horizontal circular tension crack, shown schematically in Figure 1. The crack lies above the explosion and opens when the free-surface rarefaction from the explosion encounters the crack. The material above the crack is assumed to fly straight up and return under the influence of gravity alone.

We have extended the circular tension crack model of Day, *et al.* (1983) to include a time dependence which describes the detachment and slap-down of the spall volume as well as the finite size (radius) of the crack. The spall volume in the model is defined as the cylinder whose radius is that of the tension crack and which extends from the crack to the surface. Since we wish to compare the spall model with 2D simulations which were done in a layered medium, we developed the formalism for computing the far-field body waves emanating from a layered medium. The parameters of the model are the crack radius and depth, and the distribution of detachment velocities over the crack.

In this section, we present the complete body wave formalism. We then make some simplifying assumptions to make important features of the time history and spectrum apparent.

We begin with the representation theorem from Aki and Richards (1980), which describes the displacement field due to a discontinuity on a surface Σ :

$$u_n(x,t) = \iint_{\Sigma} m_{pq}(\xi,t) * G_{np,q}(x-\xi,t) d\Sigma \quad (1)$$

where

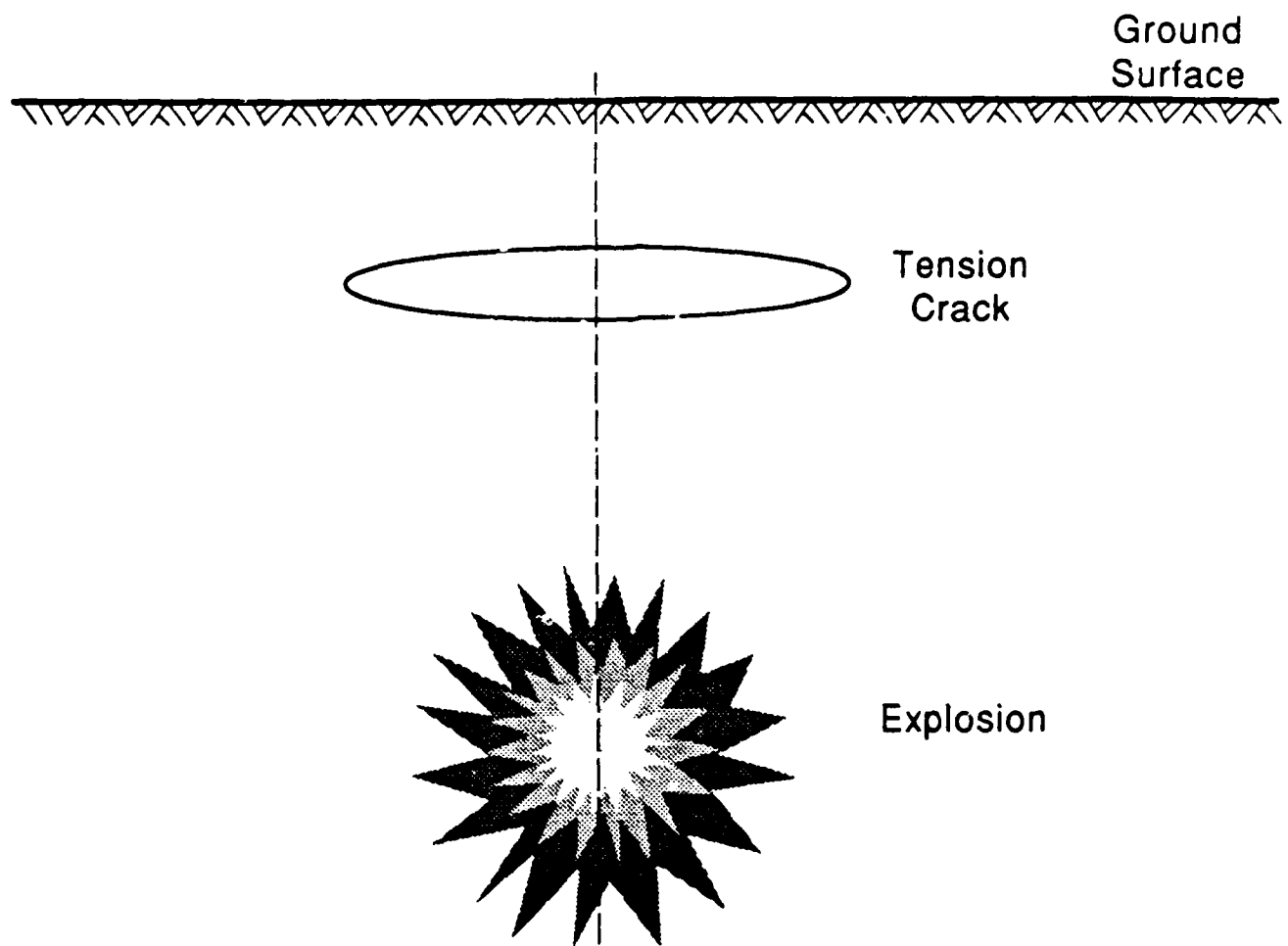


Figure 1. The tension crack model for spill from an explosion.

\underline{x} is the observer's position,

$\underline{\xi}$ is a position on Σ ,

$G_{np}(\underline{x}-\underline{\xi},t)$ is the Green's function giving the component of displacement in the x_n direction at \underline{x} due to a force in the ξ_p direction,

$G_{np,q}(\underline{x}-\underline{\xi},t)$ is the gradient of $G_{np}(\underline{x}-\underline{\xi},t)$ in the ξ_q direction,

$m_{pq}(\underline{\xi},t)$ is the moment tensor density for the discontinuity, and

* denotes temporal convolution.

For an isotropic medium, the moment tensor density is given by

$$m_{pq}(\underline{\xi},t) = \lambda v_k [u_k(\underline{\xi},t)] \delta_{pq} + \mu \left\{ v_p [u_q(\underline{\xi},t)] + v_q [u_p(\underline{\xi},t)] \right\} \quad (2)$$

where

λ and μ are the Lamé' parameters (at $\underline{\xi}$) for the medium,

$[u]$ is the slip (crack opening) along the discontinuity,

\underline{y} is the unit normal to the discontinuity, and

δ_{pq} is the Kronecker delta.

(Repeated indices indicate summation over three components). For a horizontal tension crack with opening $s(\xi_1, \xi_2, t)$,

$$\underline{y}^T = [0, 0, 1] \quad (3)$$

$$[\underline{u}]^T = [0, 0, s(\xi_1, \xi_2, t)] ,$$

and the moment tensor density is

$$m = s(\xi_1, \xi_2, t) \begin{bmatrix} \lambda & 0 & 0 \\ 0 & \lambda & 0 \\ 0 & 0 & \lambda + 2\mu \end{bmatrix} .$$

The geometry of the problem is shown in Figure 2.

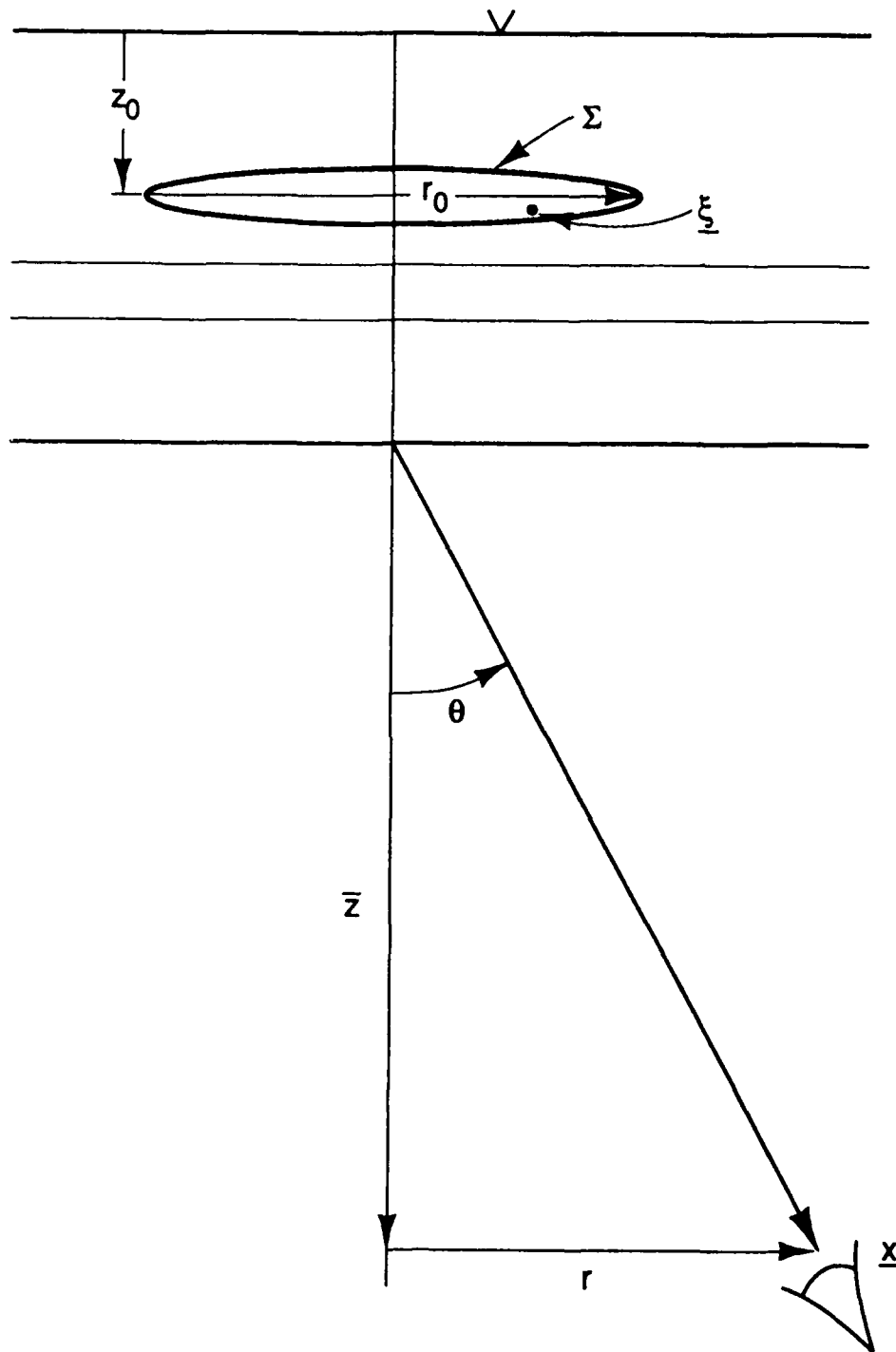


Figure 2. Geometry for a tension crack in a layered medium.

We now specify that the horizontal crack is circular with radius a and that the discontinuity varies only with distance from its center (axially symmetric). Invoking cylindrical symmetry and converting to cylindrical coordinates, the displacement field is

$$u_n(\underline{x}, t) = \int_0^{2\pi} \int_0^a \left[\lambda \frac{1}{r_0} \partial_{r_0} (r_0 G_{nr_0}) + (\lambda + 2\mu) \partial_{z_0} G_{nz_0} \right] * s(r_0, t) r_0 dr_0 d\phi \quad (4)$$

Here, r_0, ϕ, z_0 are the source cylindrical coordinates

$$\xi_1 = r_0 \cos(\phi)$$

$$\xi_2 = r_0 \sin(\phi)$$

$$\xi_3 = z_0$$

Our objective is to compute the body waves leaving a layered stack. We use the formalism of Fuchs (1966) and Bache and Harkrider (1976). The Fourier transforms of the P wave Green's functions in the notation of Fuchs are given by

$$G_{ij}^P(\underline{x}, \omega) = -\frac{k_\alpha^{-2}}{2\pi} \int_0^\infty \Delta^j K_{ij}^P e^{-ikr_{\alpha n} \bar{z}} k dk \quad (5)$$

Here, k is the wavenumber for phase velocity c , Δ^j is the downgoing wave potential amplitude due to a force in the j direction, \bar{z} is the vertical distance from the bottom of the stack to the observer,

$$r_{\alpha n} = [(c/\alpha_n)^2 - 1]^{1/2}$$

and $k_\alpha = \omega/\alpha_n$, where α_n is the P wave speed in the half-space below the stack. The details on the computation of Δ^j can be found in Fuchs' work. The kernels K_{ij}^P are

$$K_{zz}^P = -ikr_{\alpha n} J_0(k\bar{r}) \quad (6)$$

$$K_{rz}^P = -ikJ_1(k\bar{r})$$

$$K_{zr}^P = -ikr_{\alpha n} J_1(k\bar{r})$$

$$K_{rr}^P = \frac{1}{2}k [J_0(k\bar{r}) - J_2(k\bar{r})]$$

where J_v is a Bessel function of the first kind of order v . The coordinate $\bar{r} = |r - r_0|$, where r is measured from the center of the crack to the observer.

The SV Green's functions are

$$G_{ij}^{SV}(\underline{x}, \omega) = -2(\beta_n/c)^2 \frac{1}{2\pi} \int_0^\infty \omega^j K_{ij}^{SV} e^{-ikr_{\beta n} \bar{r}} k dk, \quad (7)$$

where the SV potential amplitudes are

$$K_{zz}^{SV} = J_0(k\bar{r}) \quad (8)$$

$$K_{rz}^{SV} = -ir_{\beta n} J_1(k\bar{r})$$

$$K_{zr}^{SV} = J_1(k\bar{r})$$

$$K_{rr}^{SV} = \frac{-i}{2} r_{\beta n} [J_0(k\bar{r}) - J_2(k\bar{r})]$$

Substituting (5) and (6) into (4), we have for the vertical component of the P wave

$$u_z^P(\underline{x}, t) = \frac{ir_{\alpha n}}{2\pi k_\alpha^2} \int_0^{2\pi} \int_0^a \int_0^\infty B(k, \bar{r}) e^{-ikr_{\alpha n} \bar{r}} S(\omega, r_0) k^2 r_0 dr_0 d\phi dk \quad (9)$$

where

$$B(k, \bar{r}) = \lambda \Delta^{r_0} \frac{1}{r_0} [kr_0 J_0(k\bar{r}) + (1 - r_0/\bar{r}) J_1(k\bar{r})] + (\lambda + 2\mu) \partial_{z_0} \Delta^{z_0} J_0(k\bar{r})$$

Following Fuchs (1966), we evaluate (9) using the saddle point approximation, which is valid for

$$R \equiv \sqrt{z^2 + \bar{r}^2} \gg \sqrt{z_0^2 + r_0^2}, \quad (10)$$

That is, it is good for observer distances much greater than the source radius and depth. Fuchs shows that integrals like (9) can be solved using the relation

$$\int_0^{\infty} f(k, \omega) e^{-ikr_{an}\bar{z}} J_m(k\bar{r}) dk \approx i^{m+1} f(k, \omega) e^{-ik_{an}R} r_{an} R^{-1}. \quad (11)$$

Applying this to Equation (9), we have

$$u_z^P(x, t) = \frac{C_z^P}{2\pi R} F^P(\omega, k) \int_0^{2\pi} \int_0^a e^{-ik_{an}R} S(\omega, r_0) r_0 dr_0 d\phi \quad (12)$$

where

$$F^P(\omega, k) = \lambda \Delta^{r_0} k + (\lambda + 2\mu) \partial_{z_0} \Delta^{z_0},$$

$$C_z^P = -\cos^2 \theta_P$$

and θ_P is the P wave take-off angle. The wavenumber k is evaluated at the takeoff angle; $k = \omega/c$, $c = \alpha_n / \sin(\theta_P)$. To evaluate the azimuthal integral in (12), we invoke the far-field condition (10), and approximate the slant range R with the lower order terms of its Taylor series,

$$R \approx \hat{r} - \frac{r}{\hat{r}} r_0$$

where

$$\hat{r} = \sqrt{z^2 + r^2}.$$

Referring to Figure 2, we see that

$$\frac{r}{\hat{r}} = \sin \theta_P \cos \phi,$$

so that (12) becomes

$$u_z^P(x, t) = \frac{C_z^P}{2\pi R} F^P(\omega, k) e^{-ik_{an}\hat{r}} \int_0^{2\pi} \int_0^a e^{-ikr_0 \cos \phi} S(\omega, r_0) r_0 dr_0 d\phi \quad (13)$$

Using the integral representation of the Bessel function

$$J_0(\zeta) = \frac{1}{2\pi} \int_0^{2\pi} e^{i\zeta \cos \phi} d\phi,$$

we have

$$u_z^P(x,t) = \frac{C_z^P}{R} F^P(\omega, k) e^{-ik_{\alpha n} \hat{r}} \int_0^a S(\omega, r_0) J_0(kr_0) r_0 dr_0 . \quad (14)$$

Applying the same steps to the SV Green's functions (7), we find

$$u_z^{SV}(x,t) = \frac{C_z^{SV}}{R} F^{SV}(\omega, k) e^{-ik_{\beta n} \hat{r}} \int_0^a S(\omega, r_0) J_0(kr_0) r_0 dr_0 . \quad (15)$$

where

$$F^{SV}(\omega, k) = \lambda \omega^r k + (\lambda + 2\mu) \partial_{z_0} \omega^{z_0} ,$$

$$C_z^{SV} = \sin(2\theta_{SV}) .$$

The radial integral in (14) and (15) can be evaluated numerically, or solved analytically for certain algebraic forms of $S(\omega, r_0)$. Some examples follow. First define

$$P(\omega) = \int_0^a S(\omega, r_0) J_0(kr_0) r_0 dr_0 ,$$

then for constant crack opening

$$S(\omega, r_0) = S_0(\omega) ,$$

we find

$$P(\omega) = \frac{a}{k} J_1(ka) S_0(\omega) .$$

If instead the dependence of crack opening on radius is quadratic,

$$S(\omega, r_0) = S_0(\omega) \frac{(a^2 - r_0^2)}{a^2} ,$$

$$P(\omega) = 2k^{-2} J_2(ka) S_0(\omega) . \quad (16)$$

Finally, for a Gaussian dependence,

$$S(\omega, r_0) = S_0(\omega) e^{-(r_0/a)^2}$$

$$P(\omega) = \frac{1}{2} a^2 e^{-(ka/2)^2} S_0(\omega) .$$

We note that the effective far-field source function under these assumptions is the

Hankel transform of the distribution of displacement on the tension crack. We shall refer to these means of calculating $P(\omega)$ in Section 3. We discuss next the specification of the time history $S(\omega, r_0)$.

2.2. Time History

The model presented here is based on a tension crack which opens due to a tension wave from the free surface. We assume that the material then simply behaves ballistically, and that no restoring forces in the medium add to bring the material back down to its original position. The displacement at each point on the tension crack then has the time history

$$S(t, r_0) = \begin{cases} v(r_0, t_0)\tau - \frac{1}{2}g\tau^2 & \text{for } 0 \leq \tau \leq 2v(r_0, t_0)/g \\ 0 & \text{for } \tau > 2v(r_0, t_0)/g \end{cases} \quad (17)$$

where $v(r_0, t_0)$ is the detachment velocity, $\tau = t - t_0$, t_0 is the time of initiation at r_0 and g is the acceleration due to gravity. The form of $v(r_0, t_0)$ can be regarded as a parameter of the model, and we have experimented with various forms of $v(r_0, t_0)$ while fitting the model to numerical simulations. These forms included (1) analytic distributions of initial velocities which initiate at the same instant across the crack (t_0 is constant), (2) random distributions, and (3) distributions which propagate outward with the pP phase from the explosion. The first form allows $P(\omega)$ to be evaluated analytically, as shown above in Section 2.1. $P(\omega)$ must be evaluated numerically for the third form. In this case, we set

$$t_0(r_0) = \sqrt{(2z_s + z_{\text{exp}})^2 + r_0^2} / \alpha$$

and $v(r_0)$ to some algebraic function of r_0 . As we shall see in the next section, the

analytic first form was adequate for the Shagan River simulations, while the third numerical form was required to fit the Pahute Mesa simulations.

Another approach is to view the spall opening as a stochastic process where one has only probabilistic estimates of the process. This allows us to make general statements about the far-field radiation. We assume that the detachment velocities at each point on the crack are distributed randomly between minimum and maximum velocities v_1 and v_2 according to a probability density function $\phi(v)$. We make the bounds explicit by writing

$$\phi(v) = f(v) [H(v-v_1) - H(v-v_2)]$$

where

$$\int_{v_1}^{v_2} f(v) dv = 1.$$

The estimate of the separation history is then

$$\bar{S}(t) = \int_{v_g}^{\infty} t (v - v_g) \phi(v) dv$$

where

$$v_g = \frac{1}{2}gt$$

Introducing the moments of the distribution

$$M_j(a, b) = \int_a^b v^j f(v) dv$$

the separation history can be written as

$$\begin{aligned} \bar{S}(t) = & t [M_1(v_1, v_2) - v_g] \Delta H(0, t_1) + \\ & t [M_1(v_g, v_2) - v_g M_0(v_g, v_2)] \Delta H(t_1, t_2) \end{aligned} \quad (18)$$

where

$$t_i = \frac{2v_i}{g} ,$$

and

$$\Delta H(t_1, t_2) = H(t-t_1) - H(t-t_2)$$

is a "boxcar" turning on at t_1 and off at t_2 . We have included the details of the opening history because as we shall see in the next section, the displacement for far-field waves is proportional to the second derivative of $\bar{S}(t)$, which is given by

$$\begin{aligned} \frac{d^2 \bar{S}(t)}{dt^2} = & M_1(v_1, v_2) \delta(t) - g \Delta H(0, t_1) + \\ & \left[\frac{1}{2} v_g f(v_g) - g M_0(v_g, v_2) \right] \Delta H(t_1, t_2) \end{aligned} \quad (19)$$

We note that for any distribution $\phi(v)$, the high frequency response will be dominated by the δ function term, which is proportional to the first moment, or the mean velocity of the distribution. This delta function term is the detachment phase which is followed by a free-fall dwell, which is the second term in the equation. The last term is slap down. We will discuss this equation and other features of the model in more detail in the following sub-section.

2.3. Features of the Model

In the following, we make some simplifying assumptions for the purpose of illustrating the features of the model. First, we assume that the earth model is a uniform half-space. In this case, the kernels F^P and F^{SV} become

$$F^P(\omega, k) = \frac{-i\omega}{2\alpha^2 \eta_\alpha} \left[(1-2p^2\beta^{-2}) (e^{-i\omega p} + R_{pP} e^{-i\omega p'}) + 2\beta^2 p \eta_\alpha R_{sP} e^{-i\omega p'} \right] \quad (19)$$

and

$$F^{SV}(\omega, k) = \frac{i\omega}{4\beta^2\eta_\alpha} [2p\eta_\alpha sP (e^{-i\omega s} - R_{sS} e^{-i\omega s}) - (1-2p^2\beta^{-2}) R_{pS} e^{-i\omega s}] \quad (20)$$

where $p=1/c$ is the slowness, and $\eta_\alpha^2 = \alpha^{-2} - p^2$. The travel times for the P, pP, sP, S, pS and sS phases are denoted by t_P , t_{pP} , t_{sP} , t_S , t_{pS} and t_{sS} , respectively. The variables R_{pP} , R_{sP} , R_{pS} , and R_{sS} are the corresponding free surface reflection coefficients (for potentials), given by

$$R_{pP} = [4\eta_\alpha\eta_\beta p^2 - (\beta^{-2} - 2p^2)^2] / D_R ,$$

$$R_{sP} = -4\eta_\beta (\beta^{-2} - 2p^2) / D_R ,$$

$$R_{pS} = 4\eta_\alpha (\beta^{-2} - 2p^2) / D_R ,$$

with

$$R_{sS} = R_{pP} ,$$

$$D_R = 4\eta_\alpha\eta_\beta p^2 + (\beta^{-2} - 2p^2)^2$$

Long Period Limits

We note first that the DC values of F^P and F^{SV} approach zero at least as fast as ω^2 . In addition to the factor of ω in (19) and (20), the quantities

$$(1+2p^2\beta^{-2}) (1+R_{pP}) + 2\beta^2 p \eta_\alpha R_{sP}$$

and

$$2\beta^2 p \eta_\alpha (1-R_{pS}) - (1-2p^2\beta^{-2}) R_{pS} ,$$

(the limits of the functions in brackets in (19) and (20) as $\omega \rightarrow 0$), are identically zero.

As pointed out by Day (1983), the spall process should contribute no net force or momentum.

Small Take-off Angle Approximation

Next, we restrict our attention to steep take-off angles (small θ_P and θ_{SV}).

Expanding the reflection coefficients to second order in take-off angle, we find

$$R_{pP} = -1 + \left(\frac{\beta}{\alpha}\right)^3 \theta_P^2 ,$$

$$R_{sP} = -4 \frac{\beta}{\alpha} \theta_P ,$$

$$R_{pS} = 4 \frac{\beta}{\alpha} \theta_{SV} ,$$

$$R_{sS} = -1 + \frac{\beta}{\alpha} \theta_{SV}^2 .$$

Expanding the remaining quantities in (19) and (20), we find to $O(\theta_{SV}^2)$ that

$$F^P = \frac{i\omega}{\alpha} \left\{ \left[1 - 2\left(\frac{\beta}{\alpha}\right)^2 \theta_P^2 \right] (e^{-i\omega t_P} - e^{-i\omega t_{pP}}) - 8\left(\frac{\beta}{\alpha}\right)^3 \theta_P^2 (e^{-i\omega t_{pP}} - e^{-i\omega t_{sP}}) \right\} \quad (21)$$

$$F^{SV} = \frac{i\omega}{\beta} \theta_{SV} (e^{-i\omega t_S} + e^{-i\omega t_{sS}} - 2e^{-i\omega t_{pS}}) \quad (22)$$

Axial symmetry demands that the SV motion be zero as $\theta_{SV} \rightarrow 0$, as seen in (22). For small angles, the P wave motion is dominated by the P and pP phases, which for small depths of the tension crack, appear in (21) as a numerical first difference operator.

Approximation for Periods Long Compared to Travel Time to the Surface

The values of the depth of the tension crack that we infer from the numerical simulations in Section 3 are less than 200 m. The P-pP travel time for the Pahute Mesa model is about 0.25 seconds, and less than one-half that for the Shagan River model. So for frequencies much less than about 4 Hz, $\omega(t_P - t_{pP}) \ll 1$, and

$$e^{-i\omega t_P} - e^{-i\omega t_{pP}} \approx 2i\omega \eta_{\alpha z_s} e^{-i\omega t_P} . \quad (23)$$

Then (21) becomes (to 0^{th} order in θ_P),

$$F^P = \frac{-\omega^2 z_s}{\alpha} e^{-i\omega t_P} \quad (24)$$

Recall Equation (14), for the P wave displacement. The motion along the ray is approximated by

$$u_{ray}^P(\omega) = \frac{\omega^2 z_s}{\alpha^2 R} e^{-i\omega t_P} P(\omega) \quad (25)$$

Assuming that crack opening is constant, and taking the inverse Fourier transform of (25), we obtain

$$u_{ray}^P(t) = \frac{z_s}{p^2 \alpha^2 R} [(ap)^2 - t^2]^{1/2} * \ddot{S}_0(t - t_P) \quad (26)$$

Finally, we assume that the periods of interest are also longer than ap , the time it takes for a wave to travel across the tension crack. Typical teleseismic values of p are less than 0.1 sec/km and values of a are around 1 km, so $pa < 0.1$ sec. In this case, we can write

$$p^{-2} [(ap)^2 - t^2]^{1/2} \approx \frac{1}{2} \pi a^2 \delta(t) \quad ,$$

(26) becomes

$$u_{ray}^P(t) = \frac{m_{spall}}{2(\lambda + 2\mu)R} \ddot{S}_0(t - t_P) \quad , \quad (27)$$

where $m_{spall} = \rho \pi z_s a^2$ is the mass of the material lifted by the spall process. The P-wave amplitude is then proportional to the spall mass, and the opening acceleration \ddot{S} . Recall that in Section 2.2, we proscribed the opening history for a distribution of detachment velocities. We assume the distribution is uniform ($f(v)=1$.) between velocities v_1 and v_2 , evaluate (19), and substitute the result in (27):

$$u_{ray}^P(t) = \frac{m_{spall}}{2(\lambda + 2\mu)R} [\bar{v} \delta(t') - g \Delta H(0, t_1') + \quad (28)$$

$$\frac{g}{v_2 - v_1} (-v_2 + \frac{3}{4}gt') \Delta H(t'_1, t'_2)]$$

where $t' = t - t_p$ and $\bar{v} = (v_1 + v_2)/2$. Equation (28) is shown schematically in Figure 3. The initial δ function term is proportional to $m_{spall} \bar{v}$, the mean spall momentum. The dwell term is $m_{spall} g$, the gravitational restoring force. The duration of the dwell is t_1 , and that of the slap down is $t_1 - t_2$.

The far-field SV displacement is approximated by

$$u_{ray}^{SV}(t) = \frac{\pi a^2}{\beta R} \theta_{SV} \dot{S}(t) * [\delta(t - t_S) + \delta(t - t_{SS}) - 2\delta(t - t_{pS})] \quad (29)$$

Spectral Characteristics

The spectrum of the body waves from the tension crack model is a narrowband signal. To see this, consider Equation (25). As $\omega \rightarrow 0$, $P(\omega)$ approaches a constant proportional to the area of the crack, so the far-field displacement approaches zero as ω^2 . This is the case for any type of dependence of opening on r_0 . The frequency limit depends on the details of $S(\omega, r_0)$, but we can make some general statements. Using the time dependence discussed above in Equation (19), it can be shown that at high frequencies, $S(\omega) \approx M_1(v_1, v_2)$, the mean detachment velocity. Then

$$P(\omega) \approx M_1 \int_0^a S(r_0) r_0 dr_0 .$$

For constant opening (Section 2.1), upon using the asymptotic approximation for the Bessel function,

$$u_{ray}^P(\omega) \approx \omega^{-3/2} \frac{z_s}{\alpha^2 R} e^{-i\omega r_p} P(\omega) \cos(ka - 3\pi/4) , \quad (25)$$

which rolls off at a rate of $\omega^{-3/2}$ at high frequencies. However, for a crack opening distribution which goes to zero at the edge of the crack, the roll off is faster. Consider

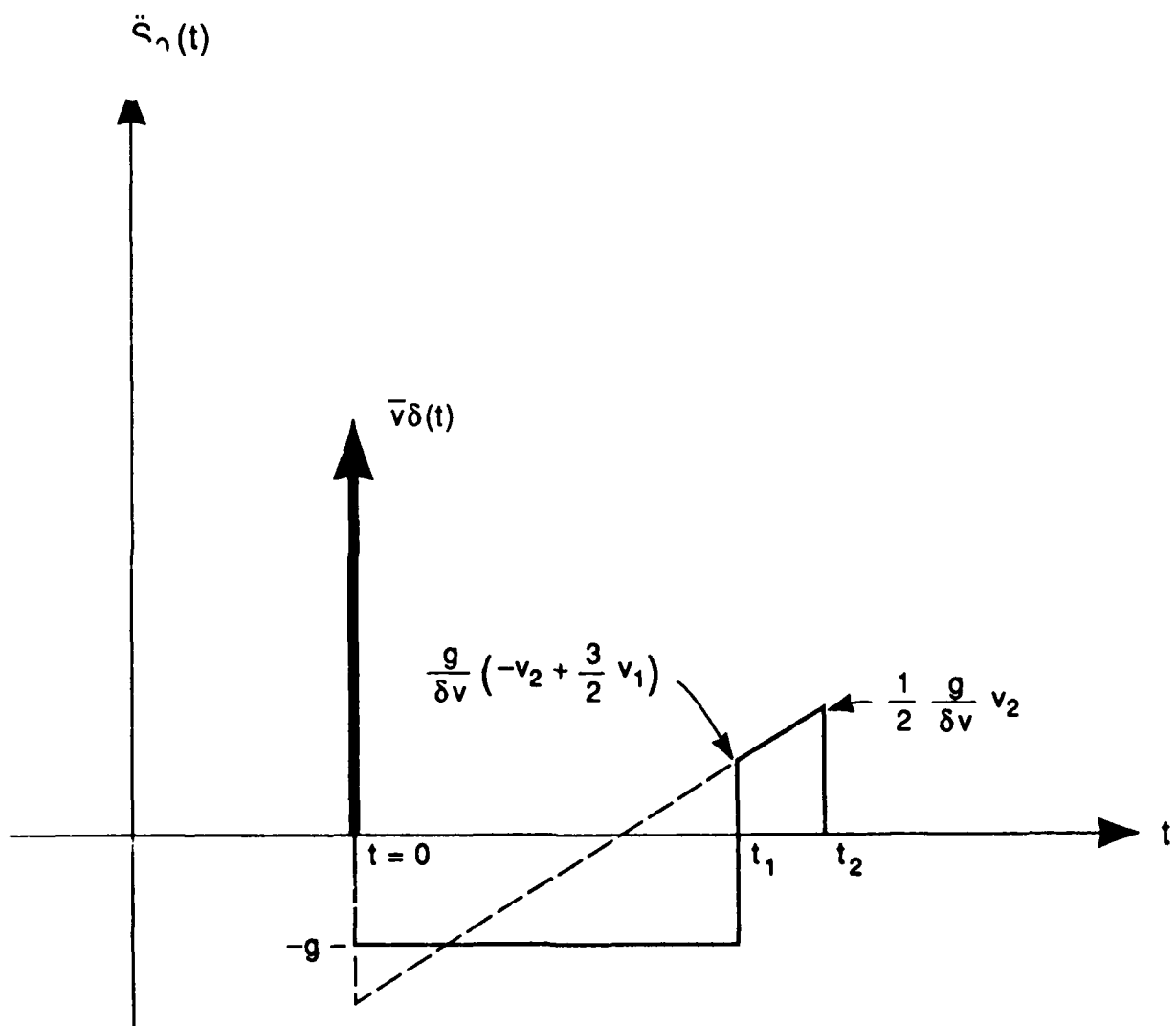


Figure 3. Schematic drawing of the detachment acceleration history which is proportional to the far-field P-wave displacement.

a distribution

$$S_0(r_0) = 1 - \left(\frac{r}{a}\right)^n ,$$

where n is a positive integer. With a little manipulation,

$$P(\omega) \approx M_1 \frac{1}{(ka)^n} \frac{n}{k^2} \int_0^{ka} \zeta^n J_1(\zeta) d\zeta ,$$

where $\zeta = kr_0$. It can be shown that at high frequencies, this expression is proportional to k^{-2} , so that the displacement rolls off at $\omega^{-5/2}$. Thus, any radial dependence which goes to zero as fast as a power of r_0 , will have a roll off of $\omega^{-5/2}$. The spectrum is shown schematically in Figure 4. Since explosion models typically decay as ω^{-2} at high frequencies, and are flat at low frequencies, the tension crack will be a more narrowband signal than the explosion by itself. Thus, if the spall contribution is comparable to that of the explosion, it will be so only in a narrowband.

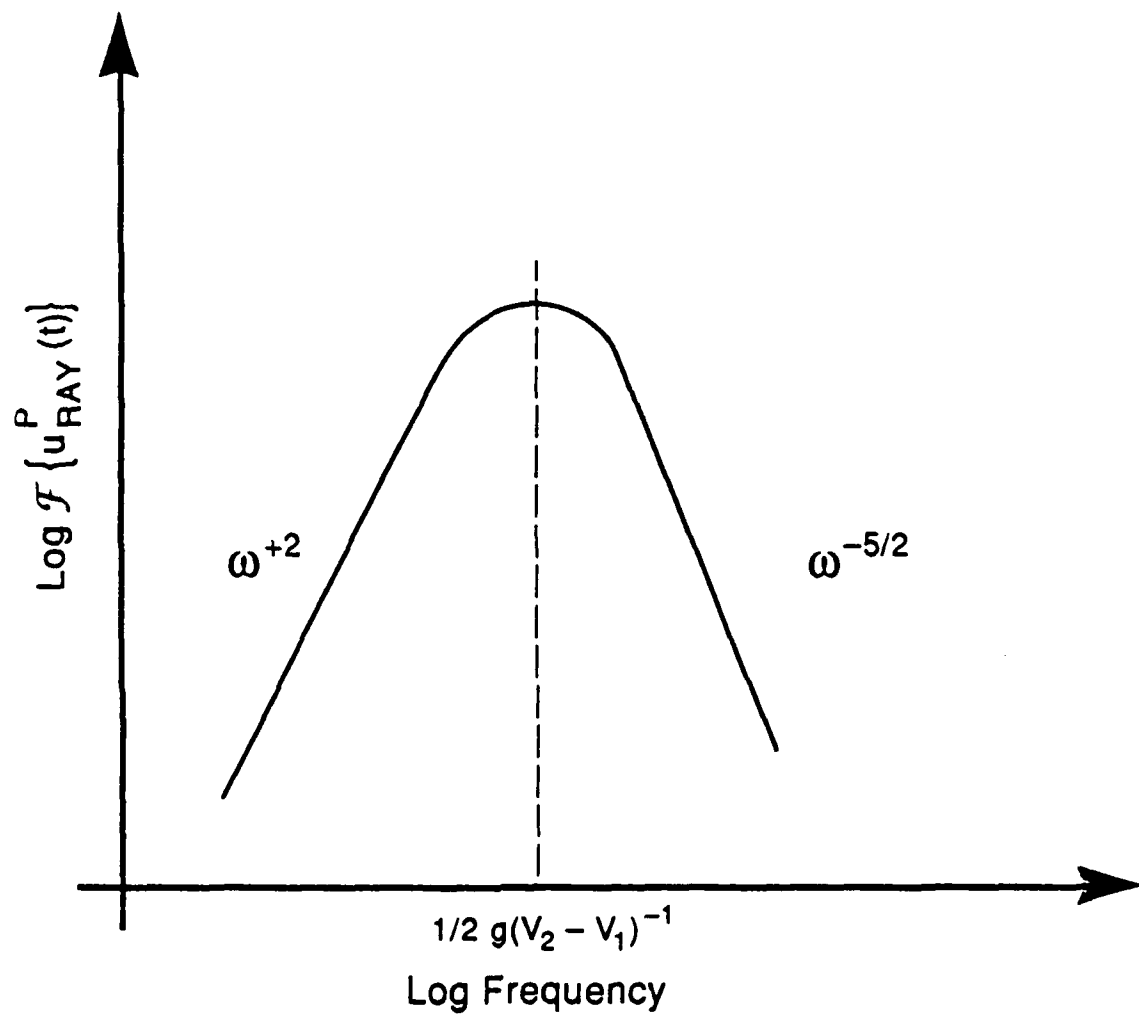


Figure 4. Schematic drawing of far-field P-wave displacement spectrum.

3. COMPARISON WITH NUMERICAL SIMULATIONS

The objective of this study was to derive a simple, linear physical model which represents the spall process. Our strategy has been to isolate source interaction effects by comparing the wavefields from 2D calculations, u_{2D} , with those from 1D calculations done, u_{1D} , in the same source materials (but in an infinite medium). Our working assumption is that the difference in the wavefields represents the free surface interaction effects, as sketched in Figure 5. In fact, the procedure has been to find the difference in the displacements $u_{2D} - u_{1D}$, and vary the parameters of the model (described in the previous section) to fit the displacements u_{spall} . Alternatively, we could have found u_{spall} which satisfies $u_{1D} + u_{spall} = u_{2D}$. We found the first approach to be more direct.

To find the ground motions from the 2D calculations, we used the methods described in Rodi, *et al.* (1978), Bache, *et al.* (1982), and Day, *et al.*, (1983, 1986). The 2D simulations themselves are described in Day, *et al.* (1986). The elastic properties for the Pahute Mesa and Shagan River simulations are shown in Table 3.1. The method for computing the body waves entails evaluating a form of the elastodynamic representation theorem, which gives the motions in terms of spatial and temporal convolutions of displacements and stresses monitored on a surface surrounding the nonlinear zone with Green's functions and their spatial gradients.

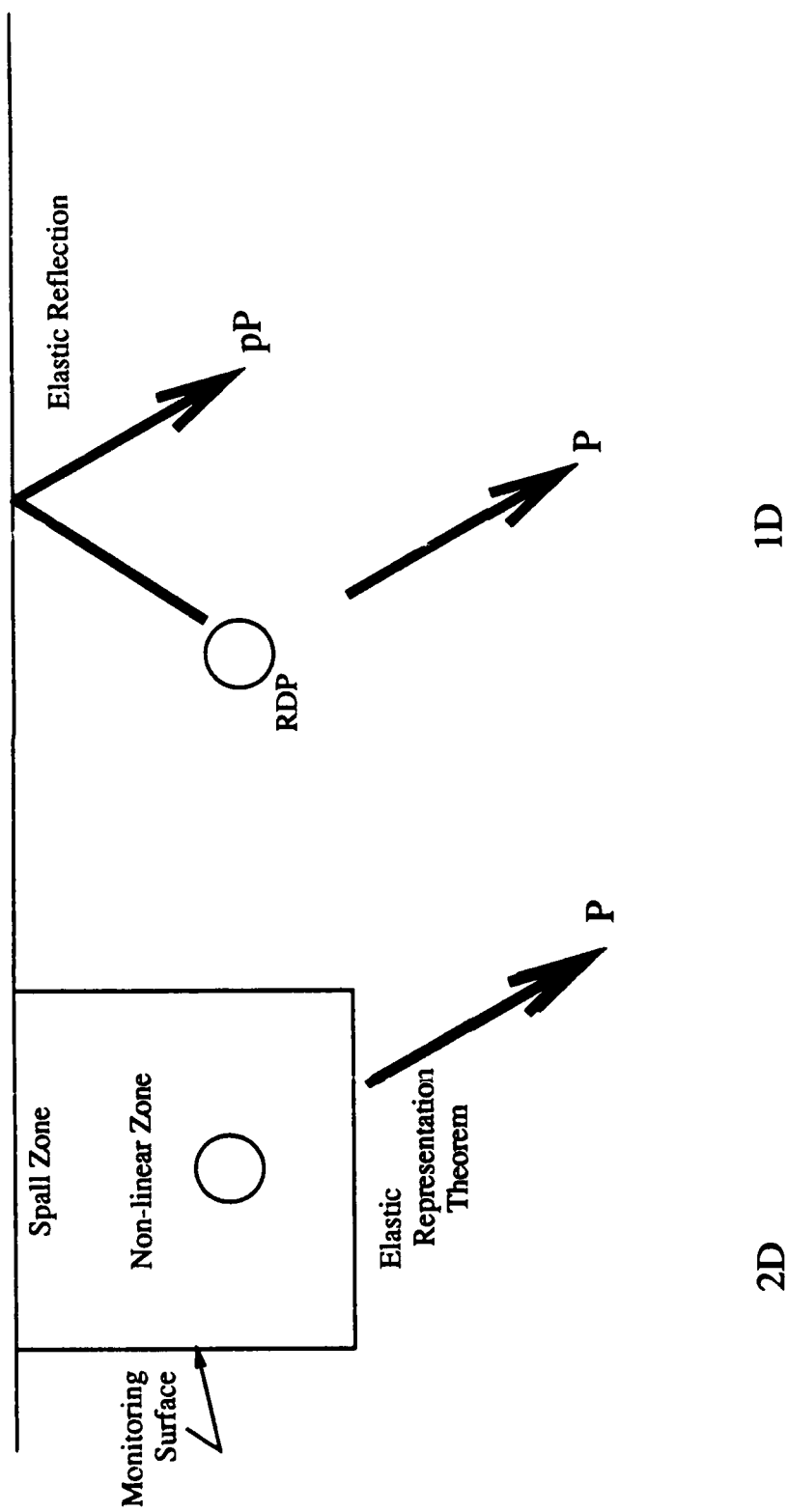


Figure 5. Sketch of the P-waves from the 2D nonlinear simulations (left) and 1D cases (right) in which an RDP (from a 1D nonlinear simulation) is embedded in an elastic medium.

Table 3.1			
Elastic Structure for the Shagan River Simulations			
Layer Thickness (m)	Compressional Velocity (m/sec)	Shear Velocity (m/sec)	Density Kg/ m ³
∞	5018	2789	2700
Elastic Structure for the Pahute Mesa Simulations			
Layer Thickness (m)	Compressional Velocity (m/sec)	Shear Velocity (m/sec)	Density Kg/ m ³
112.5	1208	661.4	1600
457.5	2025	1109	1950
∞	2887	1581	2000

3.1. Shagan River Simulations

We begin with the Shagan River simulations, which were all done at a yield of 125 KT and at three depths of burial (DOB): an over buried depth (980 m), an optimally buried depth (680 m), a depth just below cratering (no ejecta) (300 m), and a depth which causes cratering (200 m). The results for P waves were presented in Day, *et al.* (1986), and we include them here for purposes of comparing with the spall model. As can be seen in Table 3.1, the earth model is a half-space, with material properties representing typical values for the high velocity near surface media at the site. The far-field P and SV displacements are shown for three take-off angles in Figures 6 to 11. The take-off angles, 10°, 20° and 30°, are representative of teleseismic, intermediate and regional slownesses (phase velocities) for this source structure. The motions from the 2D simulations are overlain with 1D simulations in which the non-linear properties at the source are the same as the 2D values. The 1D source (RDP) was inferred, and the body waves were calculated for a linear elastic medium. Thus, for the Shagan River half-space model, the 1D waveforms have the direct P phase, as

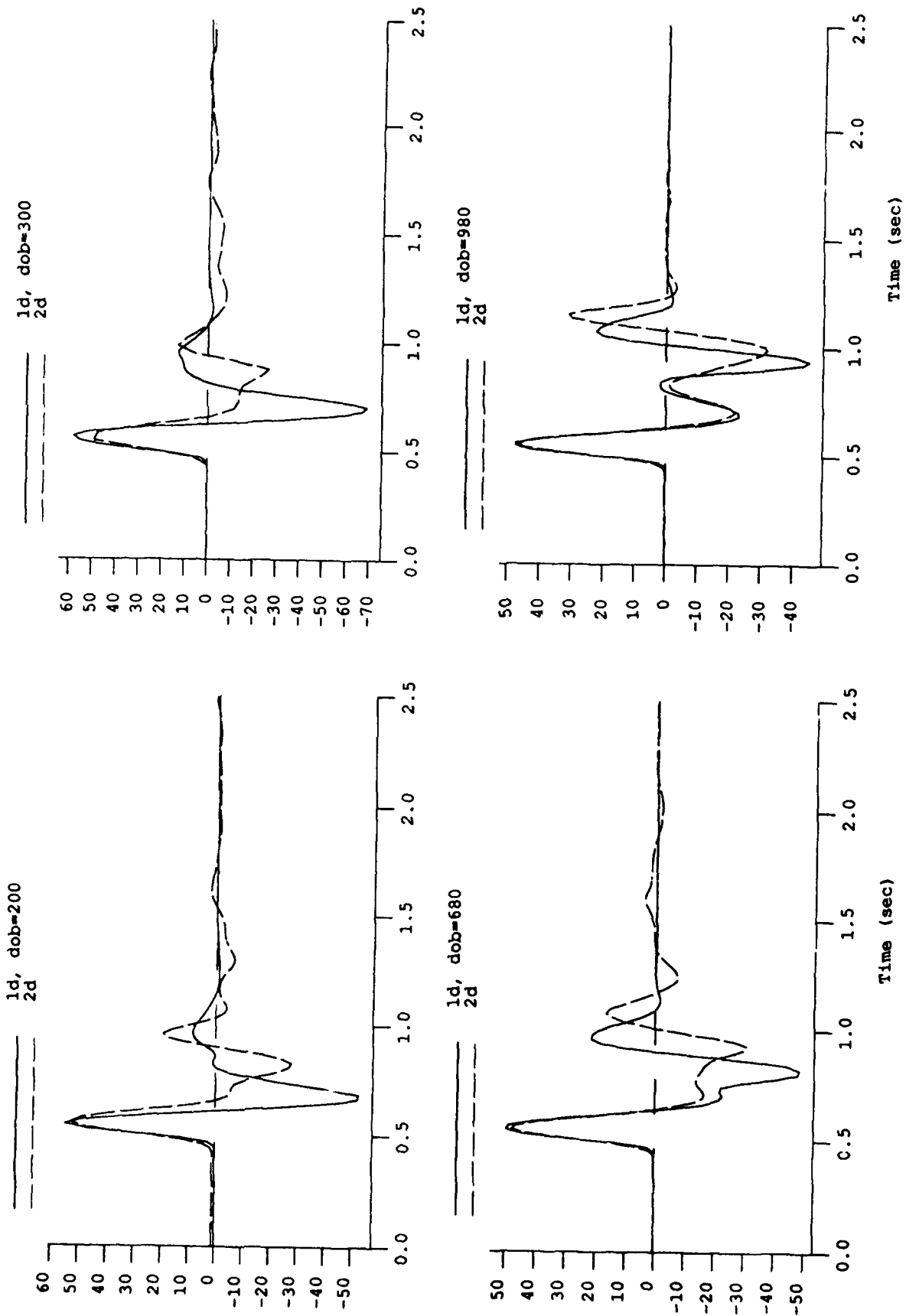


Figure 6. Comparison of the far-field P-waves from the 1D (solid lines) and 2D (dashed lines) Shagan River simulations for four depths of burial at a take-off angle of 10° .

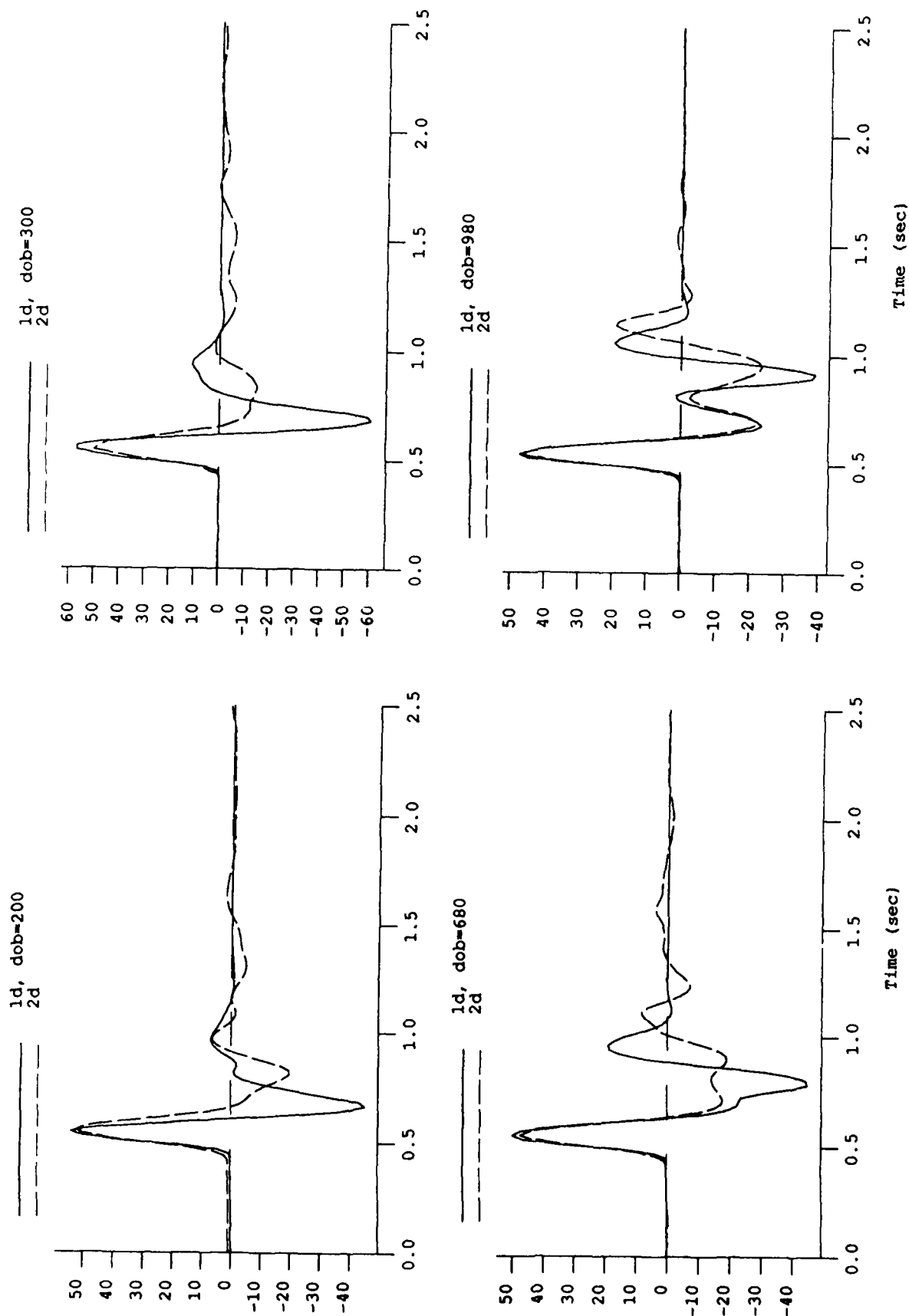


Figure 7. Comparison of the far-field P-waves from the 1D (solid lines) and 2D (dashed lines) Shagan River simulations for four depths of burial at a take-off angle of 20° .

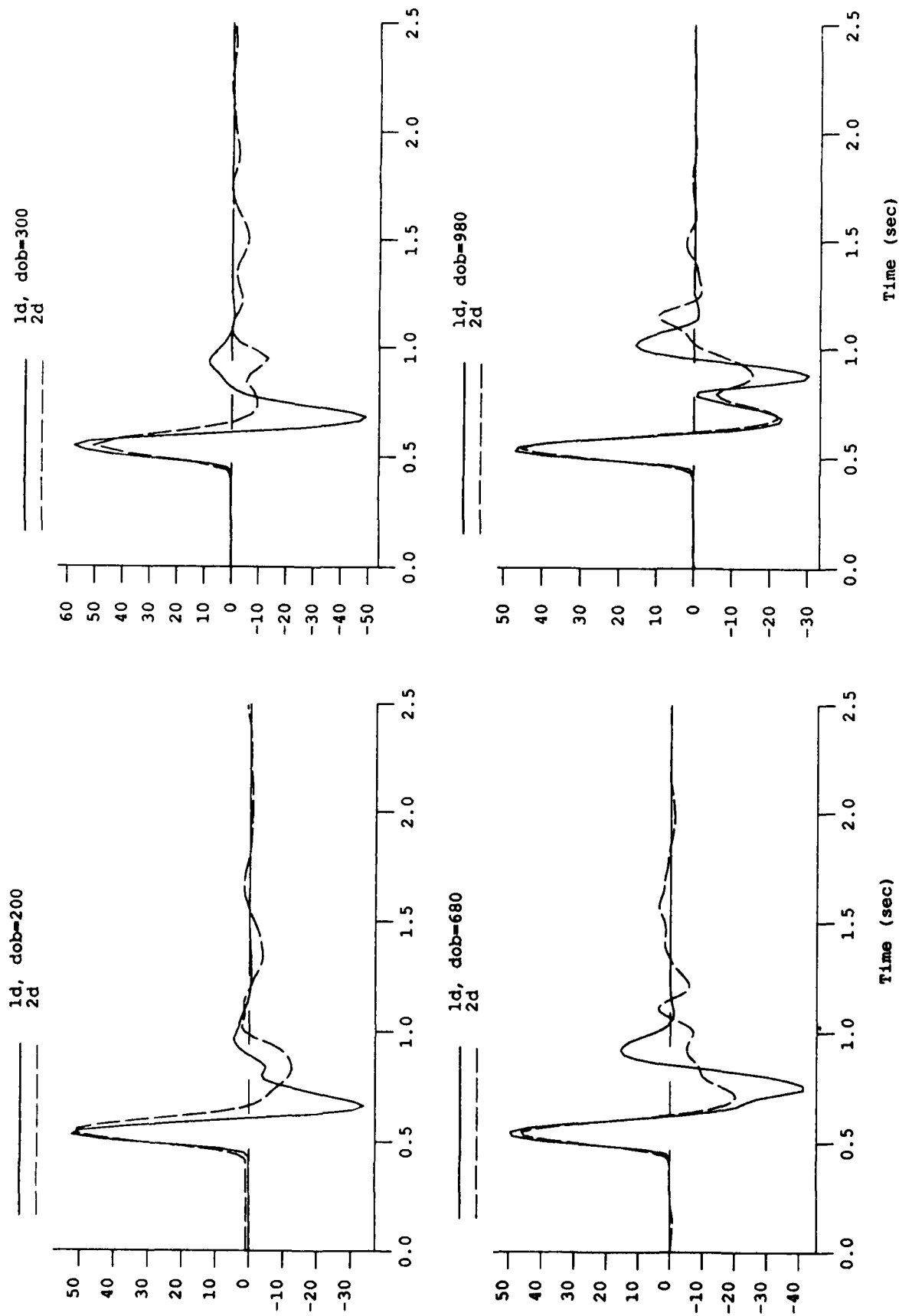


Figure 8. Comparison of the far-field P-waves from the 1D (solid lines) and 2D (dashed lines) Shagan River simulations for four depths of burial at a take-off angle of 30° .

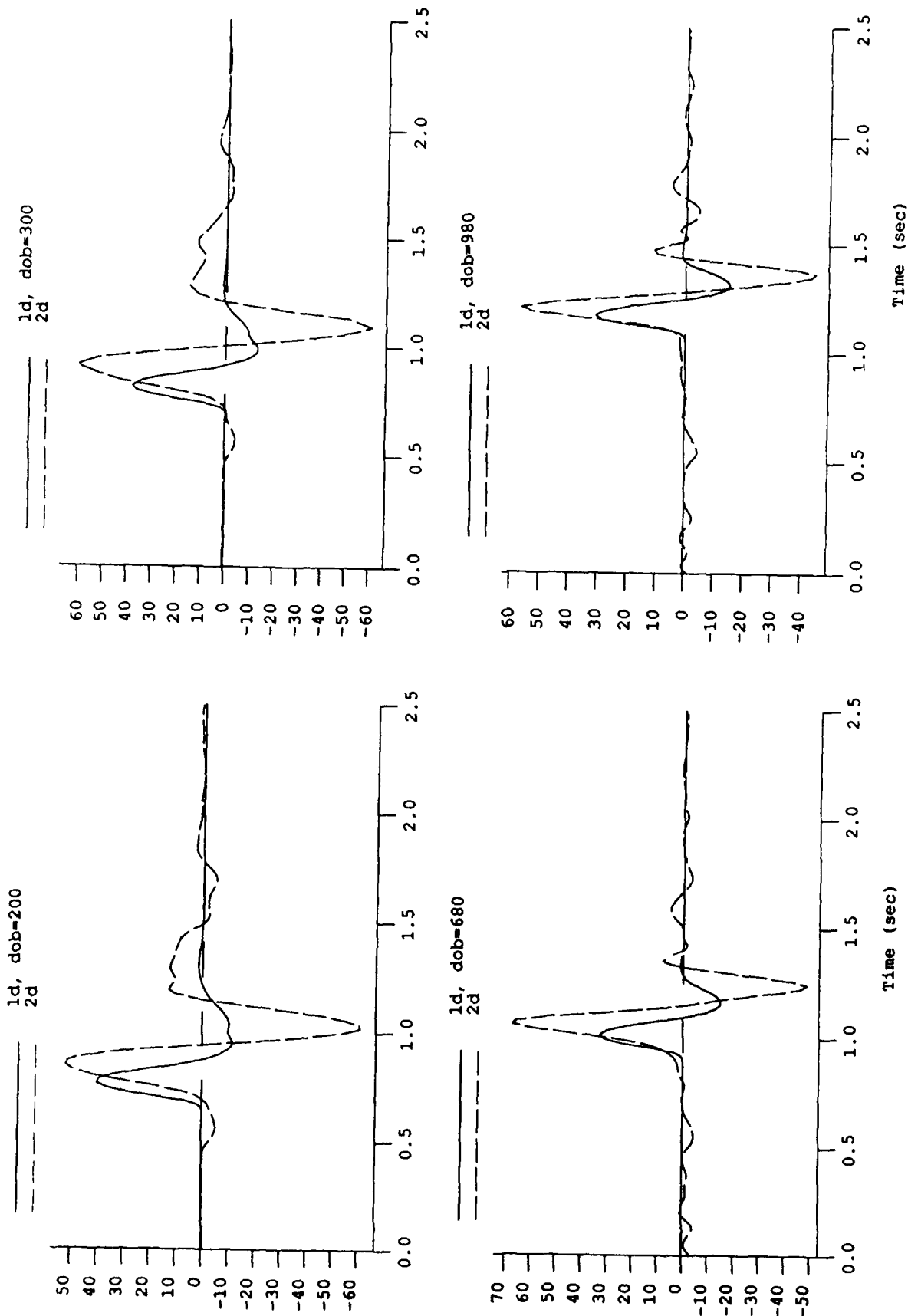


Figure 9. Comparison of the far-field SV-waves from the 1D (solid lines) and 2D (dashed lines) Shagan River simulations for four depths of burial at a take-off angle of 10° .

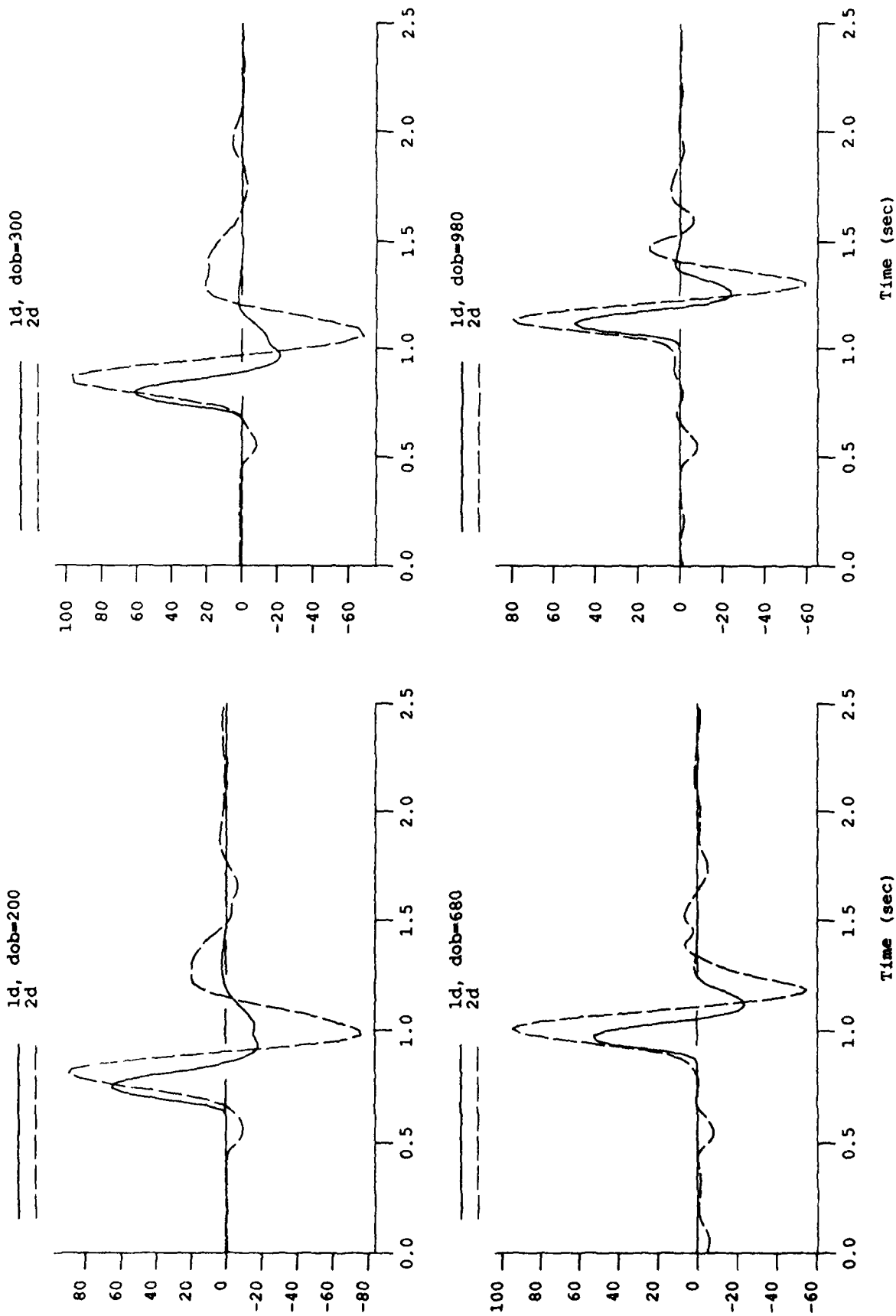


Figure 10. Comparison of the far-field SV-waves from the 1D (solid lines) and 2D (dashed lines) Shagan River simulations for four depths of burial at a take-off angle of 20°.

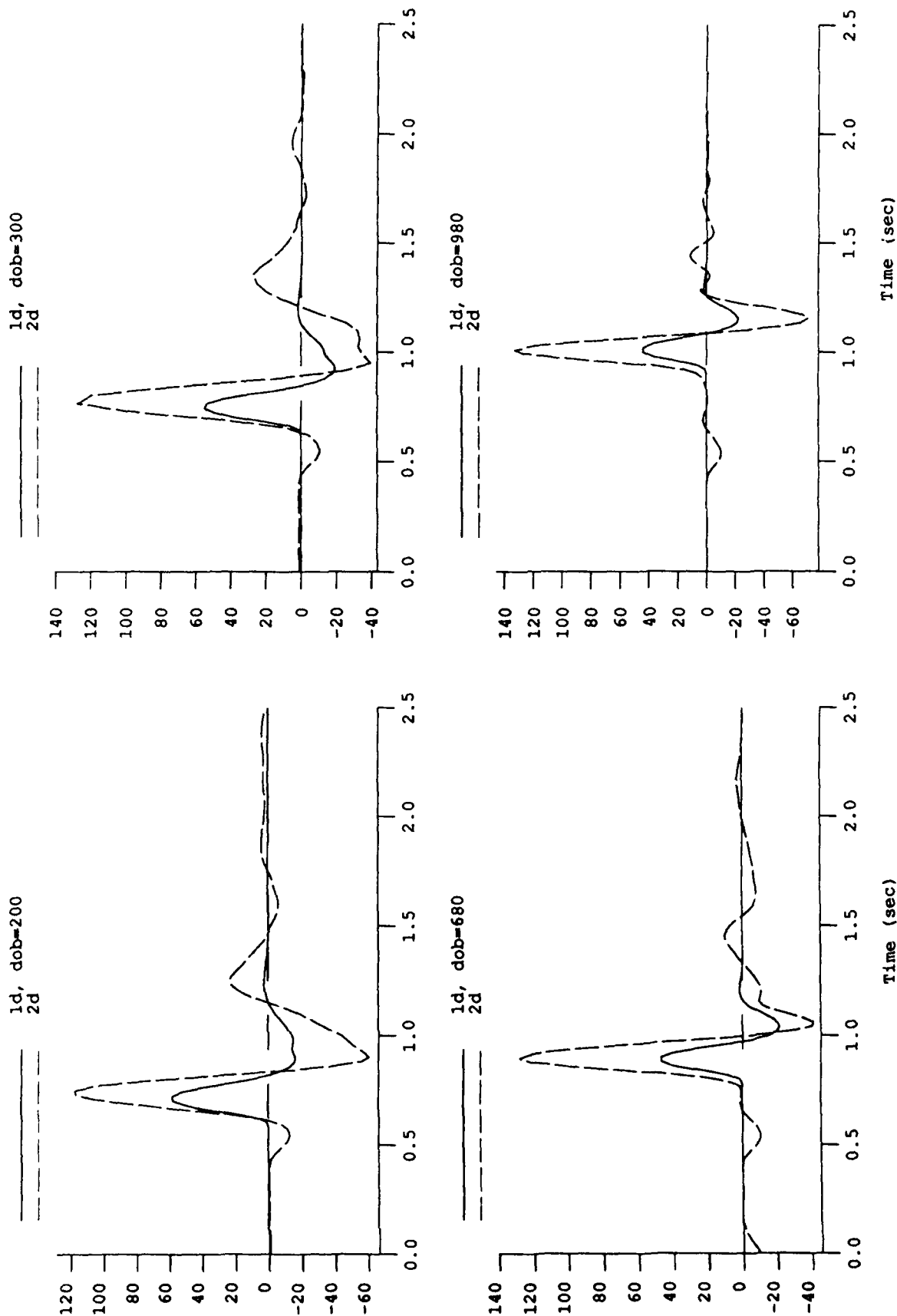


Figure 11. Comparison of the far-field SV-waves from the 1D (solid lines) and 2D (dashed lines) Shagan River simulations for four depths of burial at a take-off angle of 30° .

well as the pP and pS elastic reflections. These signals do not include the effects of mantle or crustal propagation, anelastic attenuation, or recording instrumentation.

In each case, the rise time and amplitude of the first peak in the P waves (Figures 6-8) is very nearly the same for the 1D and 2D calculations. For the shallow calculations, 200 and 300 m, the 1D and 2D waveforms diverge after the peak and are quite different at later times, indicating that the cratering and near-cratering processes are indeed different from elastic pP reflections. For the deeper DOB's, 680 and 980 m, the apparent pP phase on the 2D records appears to be diminished and delayed relative to the 1D case.

The SV waves (Figures 9-11) show much greater differences between the 1D and 2D cases. The 2D solutions have a direct S wave, due to vertical asymmetries in the source, which is not in the 1D solutions. The main peaks in the 2D SV waves are larger than the 1D peaks at all four DOB's, and are about twice as big for 300, 680 and 980 depths. The duration of the main peaks is also greater for the 2D cases. A large negative swing occurs on the 2D waveforms, which is much smaller on the 1D signals.

As discussed above, we computed the 2D-1D waveforms and matched them to those from the spall model. The parameters of the spall model which most closely matched the numerical simulations are:

Table 3.2 Spall Model Parameters for the Shagan River Simulations				
Depth of Burial	Crack Depth	Crack Radius	Minimum Detachment Velocity	Maximum Detachment Velocity
z_{exp} (m)	z_s (m)	a (m)	v_1 (m/sec)	v_2 (m/sec)
200	100	600	1.1	20.0
300	150	600	1.1	15.0
680	200	600	1.1	4.0
980	200	600	1.1	1.5

The theoretical waveforms were found to be weakly dependent on the form of the source function $S(\omega, r_0)$ in this case, so it was assumed constant. In Figures 12 through 15, we compare the P wave spall model waveforms with the 2D-1D waveforms for each of the DOB's. In general, the comparisons are quite good, both in amplitude and shape. The parameter that varies the most in Table 3.2 is the maximum detachment velocity v_2 . Recall that in Equation (28), Section 2.3, v_2 enters the solution in two ways. First, the δ function term, which causes the first peak in the waveforms, is proportional to the mean detachment velocity \bar{v} . Second, the duration of the signal (end of slap-down) is time $t_2 = 2v_2/g$. As the DOB decreases, the 2D-1D difference waveforms increase in amplitude and duration. Thus, as the DOB decreases, v_2 is required to increase. We note that, even in the case where cratering occurred (200 m), the tension crack model provided a good representation of the P radiation. The shapes of the signals for the 980 m case agree well. For the 680 m case, the agreement is good except for an additional inflection in the later parts of the 2D waveforms that is not modeled by the tension crack.

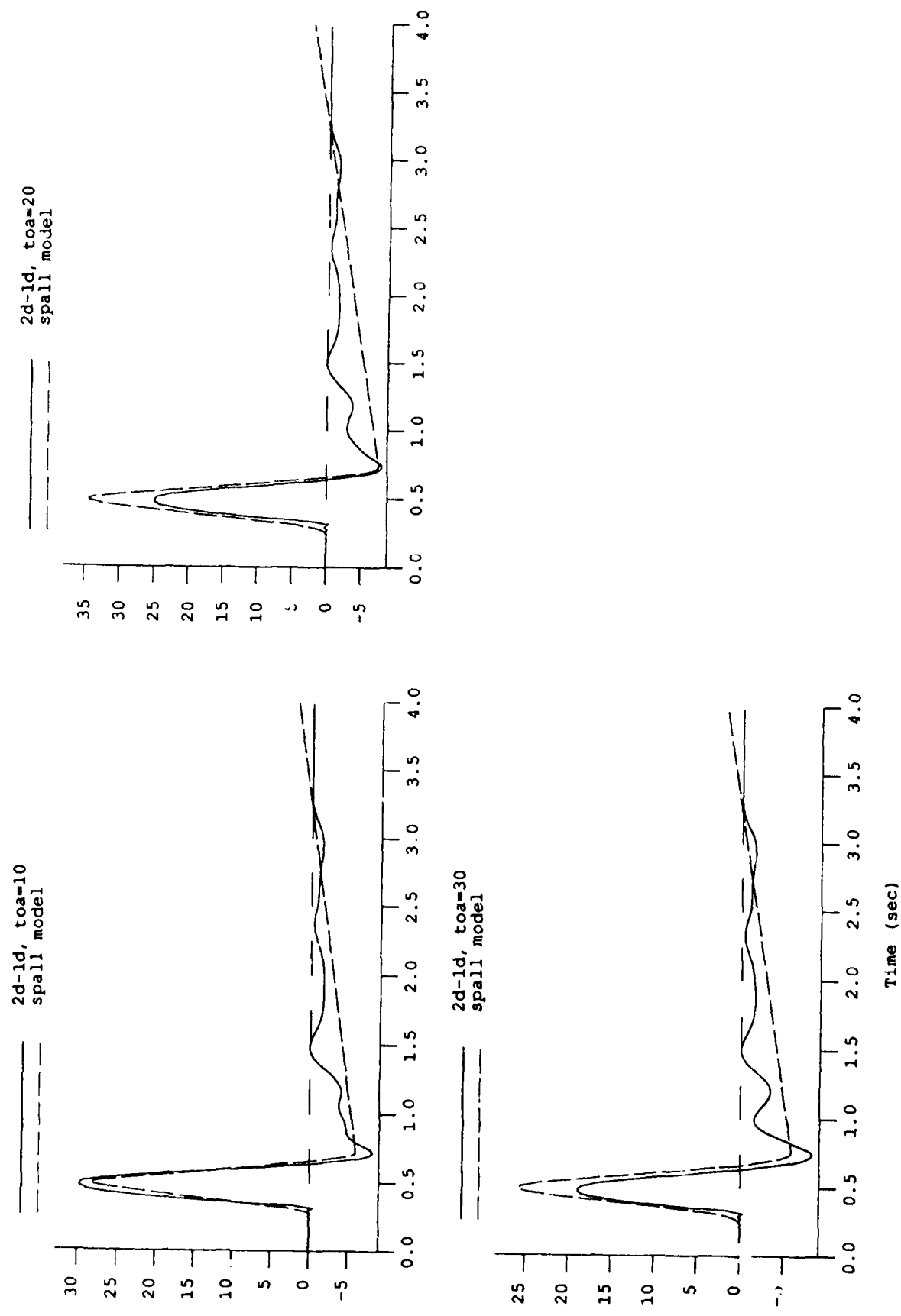


Figure 12. Comparison of the far-field P-waves from the 2D-1D (solid lines) Shagan River simulations with the tension crack model (dashed lines) at three take-off angles for a depth of burial of 200 m.

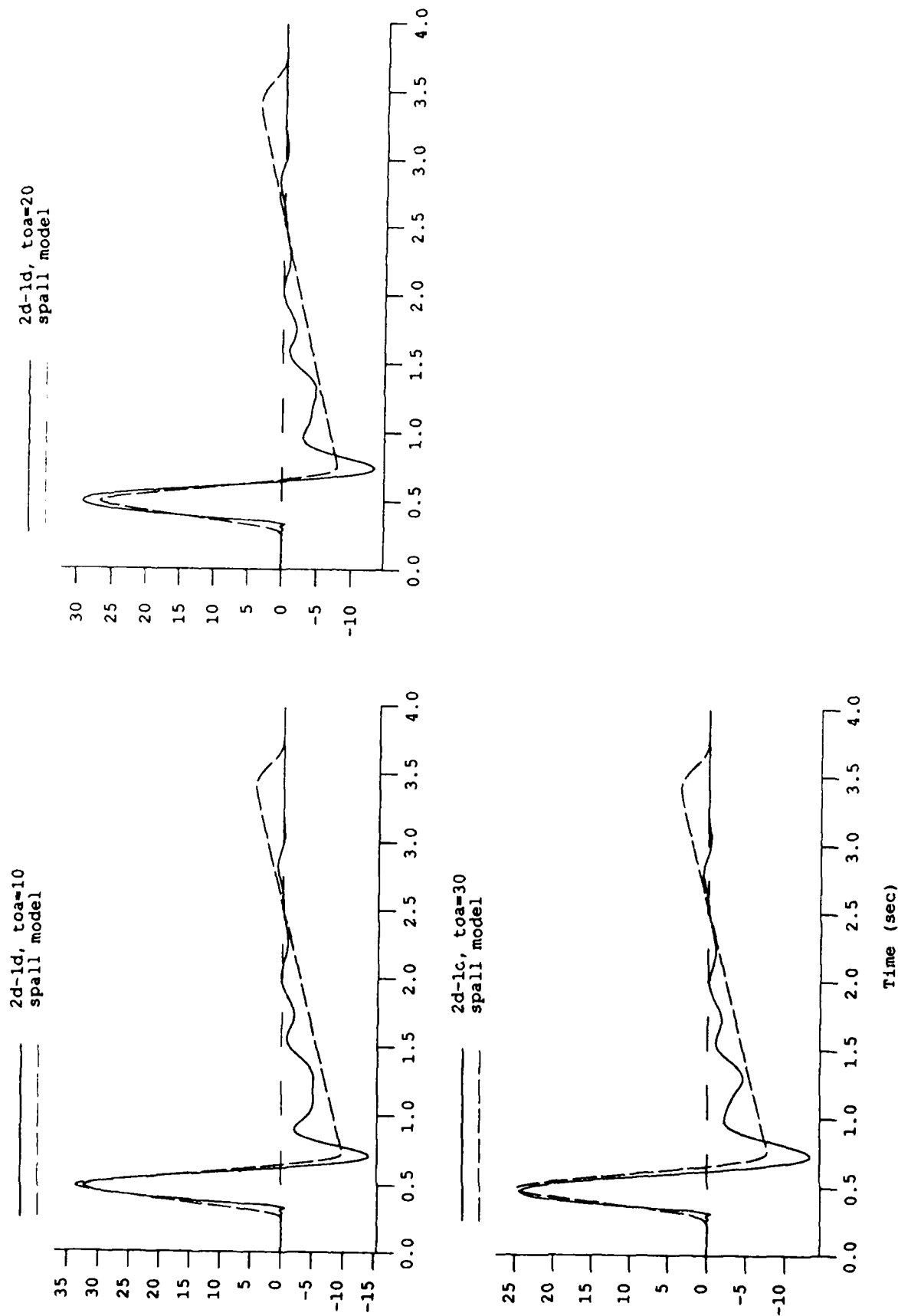


Figure 13. Comparison of the far-field P-waves from the 2D-1D (solid lines) Shagan River simulations with the tension crack model (dashed lines) at three take-off angles for a depth of burial of 300 m.

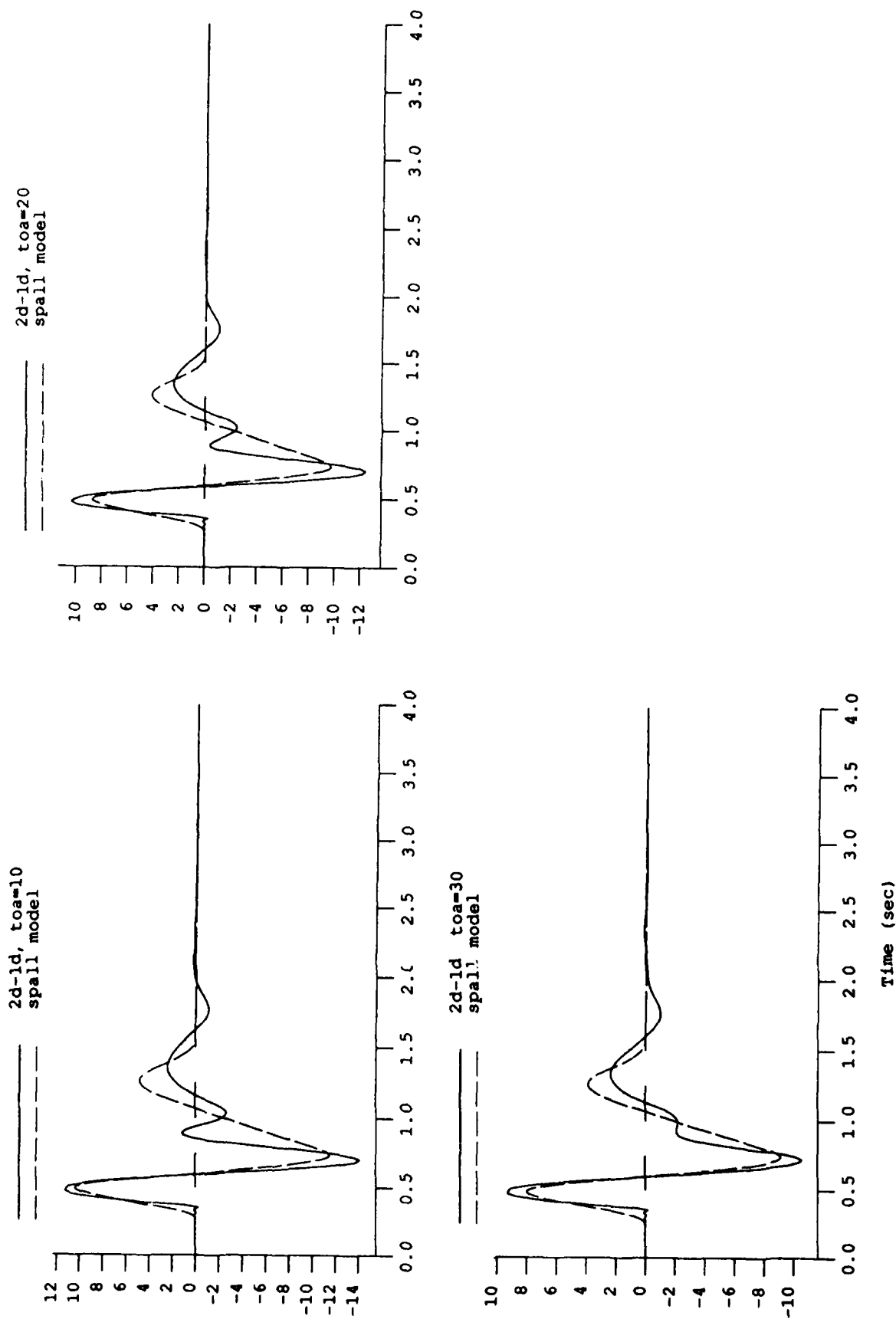


Figure 14. Comparison of the far-field P-waves from the 2D-1D (solid lines) Shagan River simulations with the tension crack model (dashed lines) at three take-off angles for a depth of burial of 680 m.

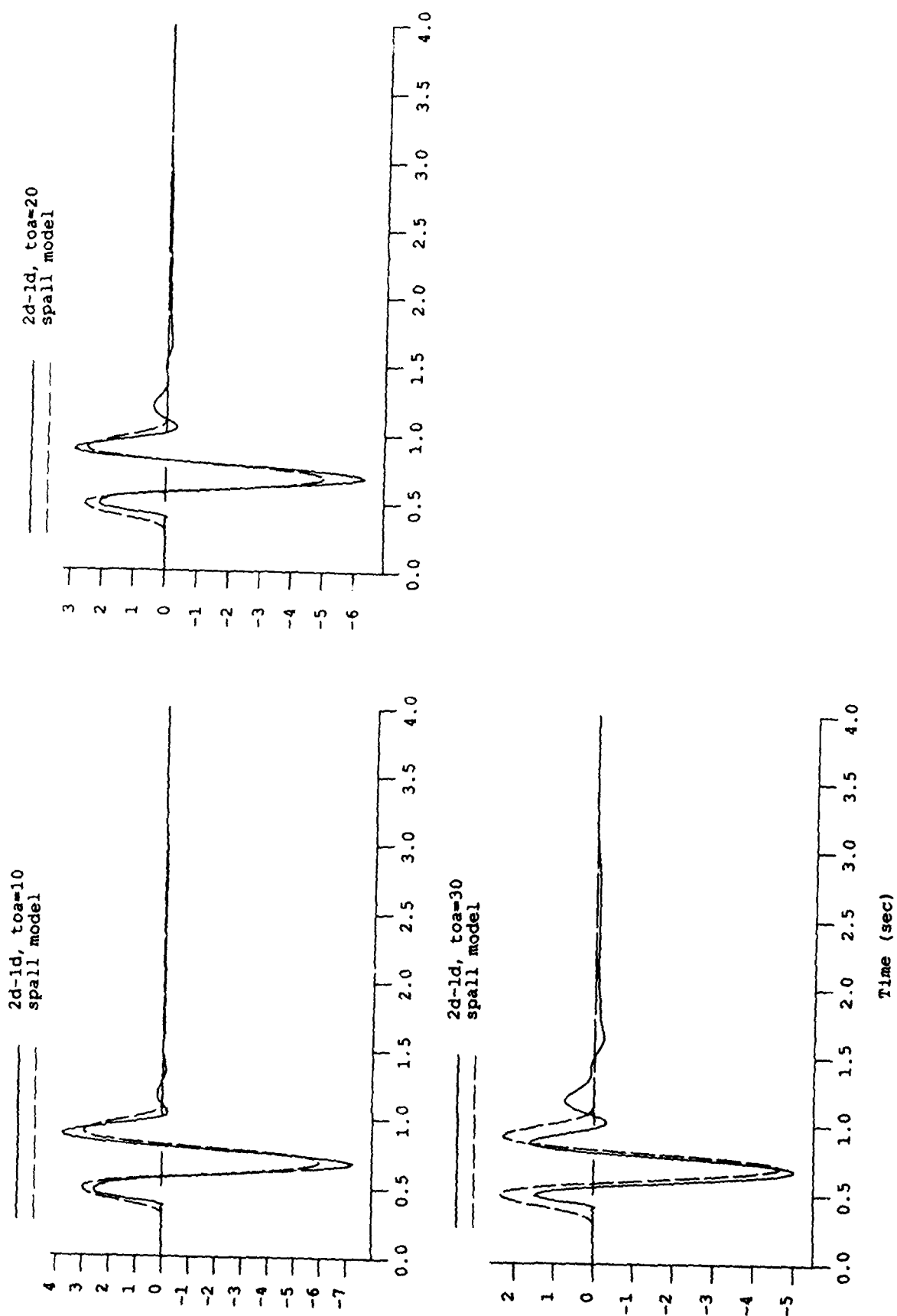


Figure 15. Comparison of the far-field P-waves from the 2D-1D (solid lines) Shagan River simulations with the tension crack model (dashed lines) at three take-off angles for a depth of burial of 980 m.

The peak detachment velocity is inferred from field observations from ground motion records at or near ground zero. We can do an analogous measurement by examining the vertical velocity in the finite difference simulation at the free-surface of the grid. We find that the values of v_2 in Table 2.2 agree closely with the ground zero velocities in the simulations.

Using the parameters in Table 3.2, we computed the SV waves from the tension crack model and compared them with the corresponding 2D-1D SV waves. As can be seen in Figures 16 to 19, the comparisons are not as good as the P-waves, especially at the deeper DOB's, where the amplitudes predicted by the model are too small by factors of two to three. Attempts to find a set of parameters which would improve the SV comparisons without degrading the P comparisons were unsuccessful. We note that in all cases, the tension crack models derived from the P-waves underestimate the SV radiation.

The results of the SV comparisons suggest that the tension crack model is not rich enough in SV radiation. We therefore tried some additions to the model to improve this situation. The additions, a compensated linear vector dipole and a distributed double-couple, are pictured in Figure 20. We hypothesized that processes transpired in the simulations that could be represented as modifications to the isotropic part of the moment tensor. We first chose to represent this as a compensated linear vector dipole or CLVD (e.g., Knopoff and Randall, 1970). The CLVD represents a process akin to squeezing a vertical tube of toothpaste. The moment density for the CLVD is given by

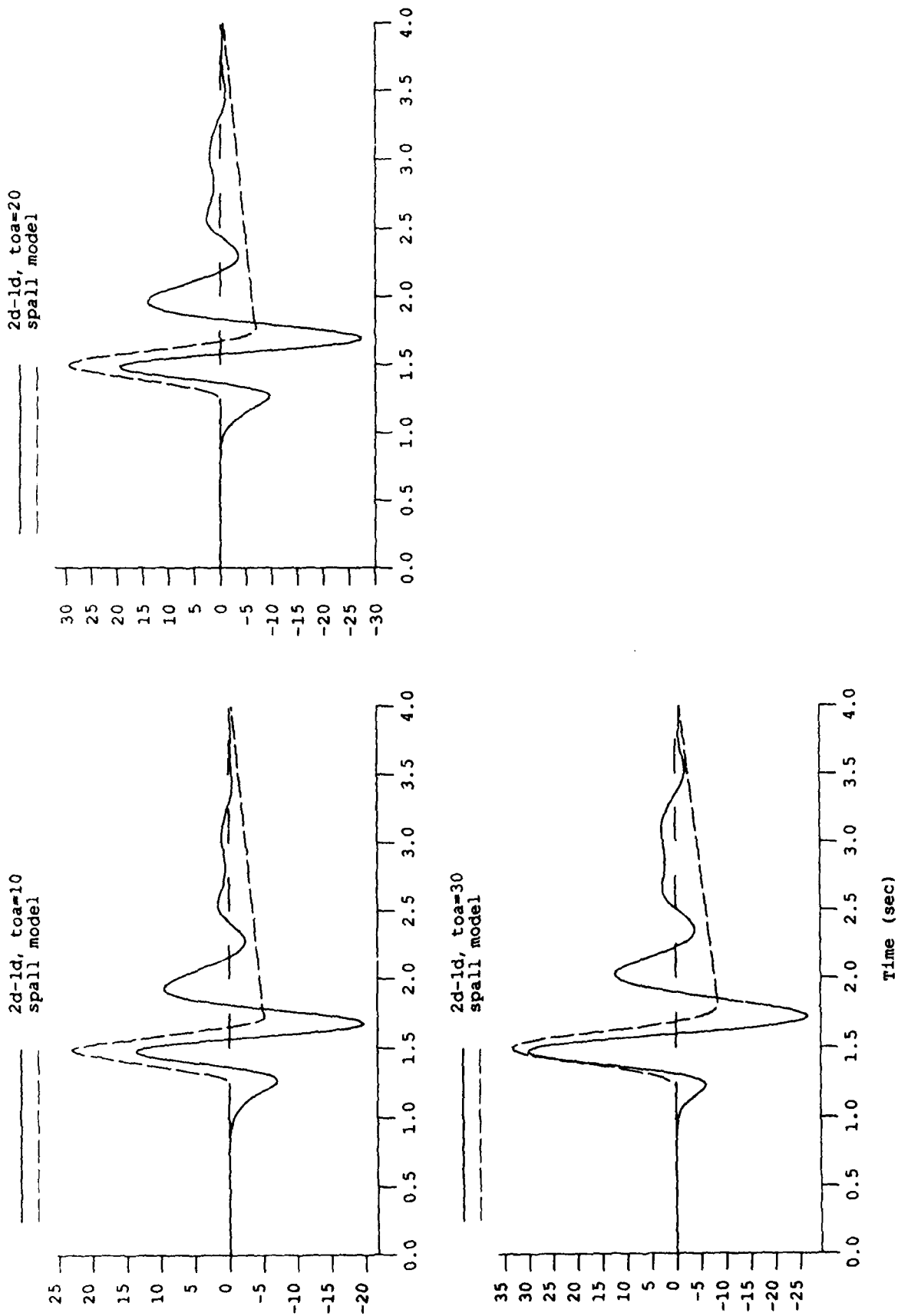


Figure 16. Comparison of the far-field SV-waves from the 2D-1D (solid lines) Shagan River simulations with the tension crack model (dashed lines) at three take-off angles for a depth of burial of 200 m.

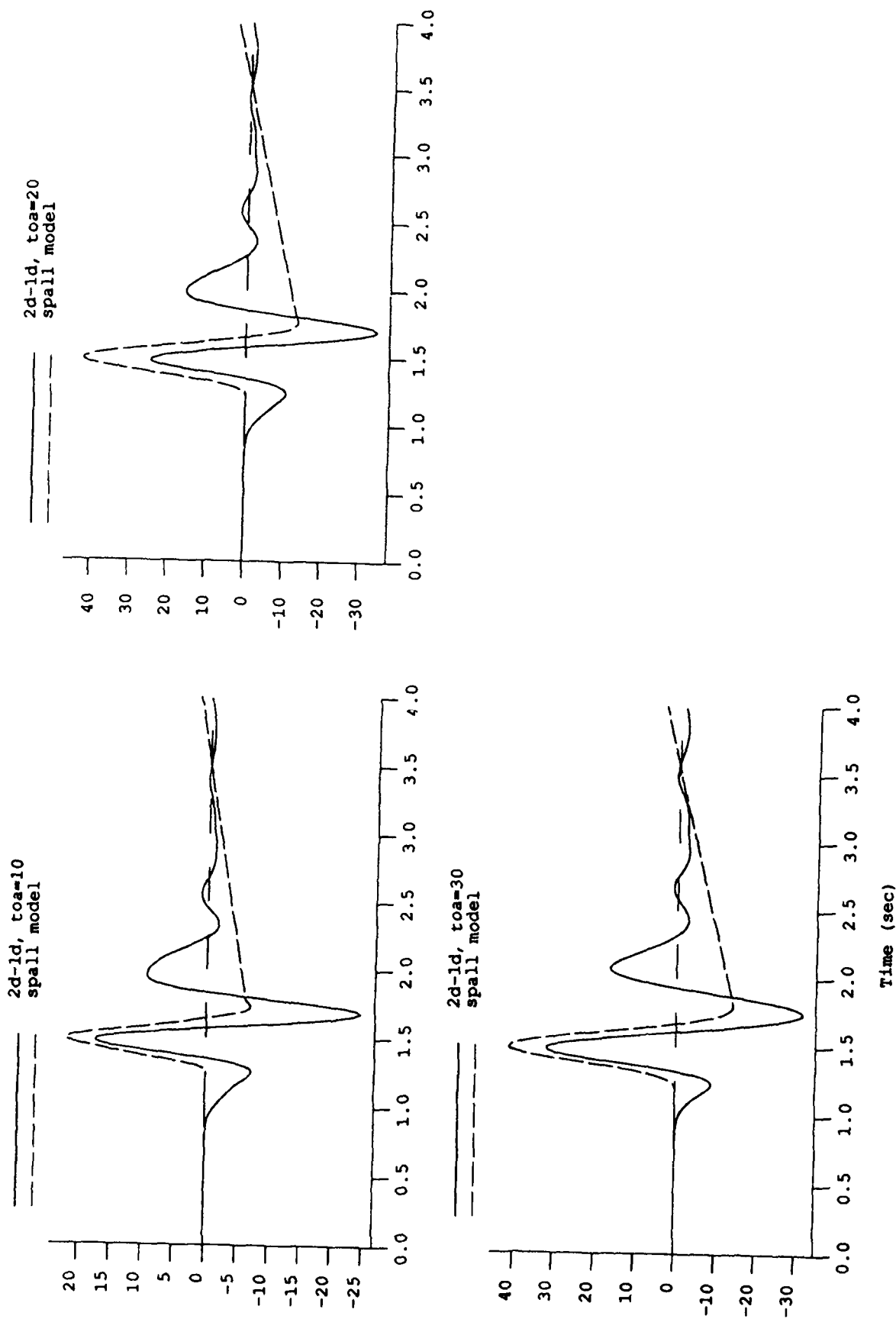


Figure 17. Comparison of the far-field SV-waves from the 2D-1D (solid lines) Shagan River simulations with the tension crack model (dashed lines) at three take-off angles for a depth of burial of 300 m.

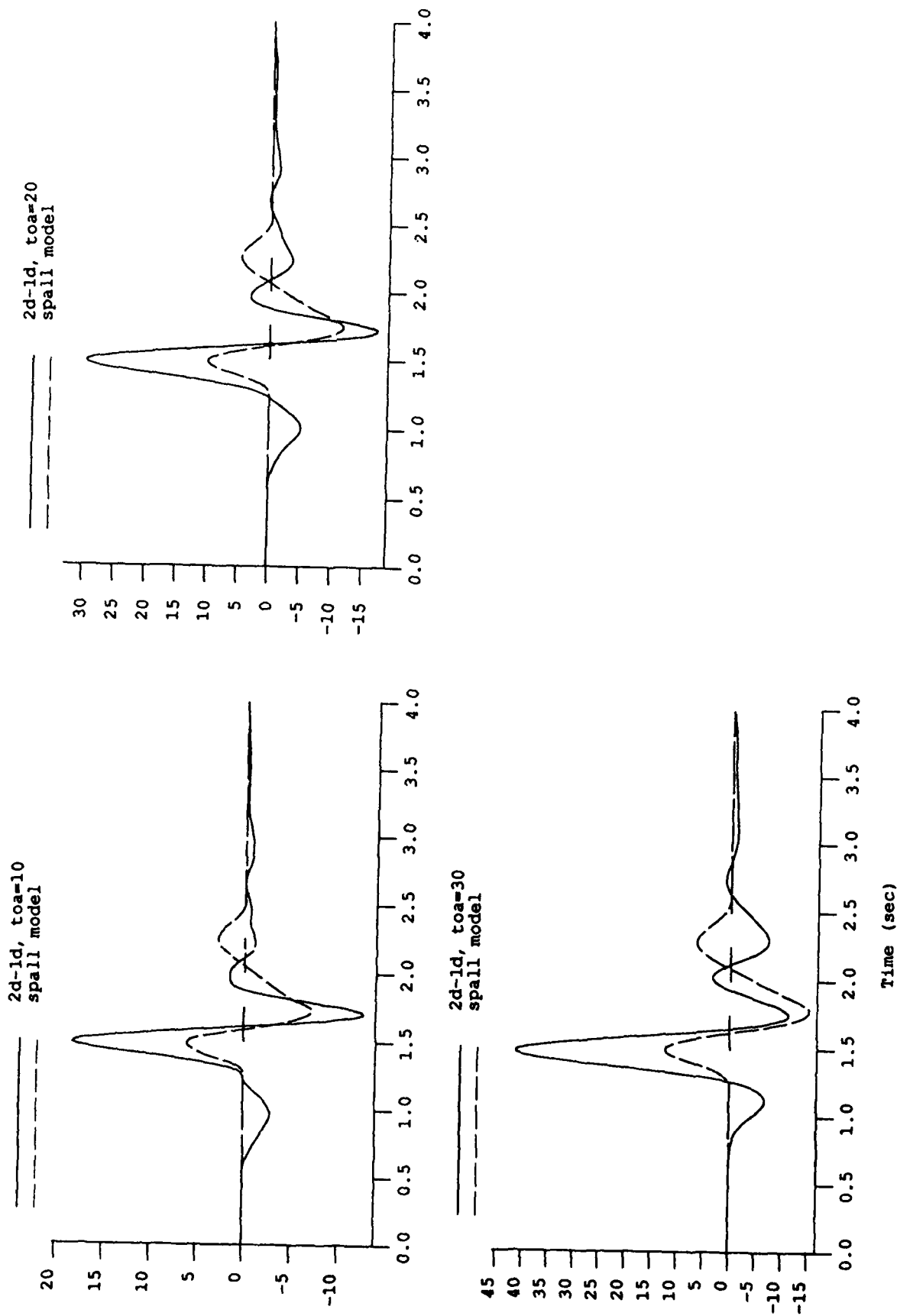


Figure 18. Comparison of the far-field SV-waves from the 2D-1D (solid lines) Shagan River simulations with the tension crack model (dashed lines) at three take-off angles for a depth of burial of 680 m.

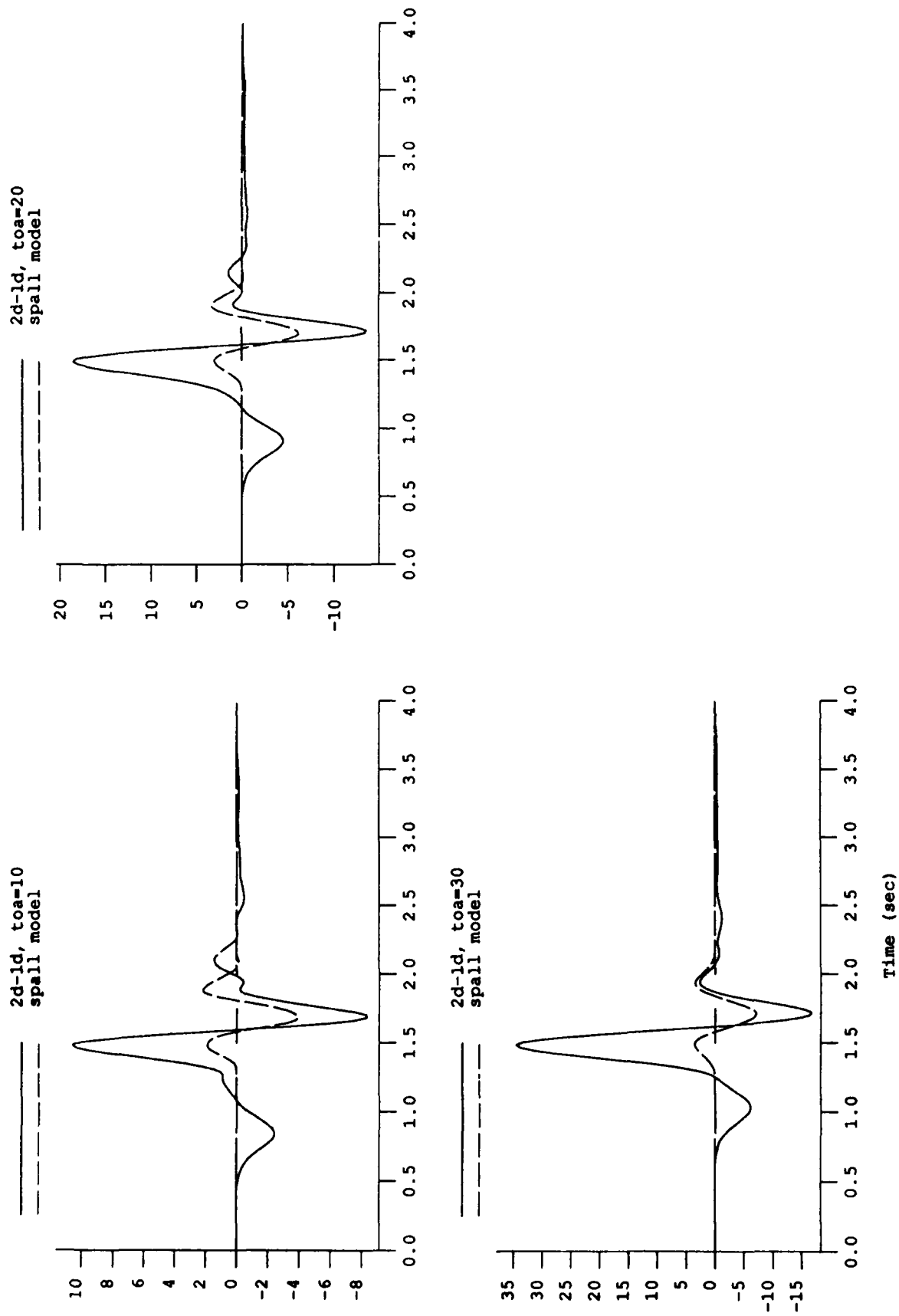
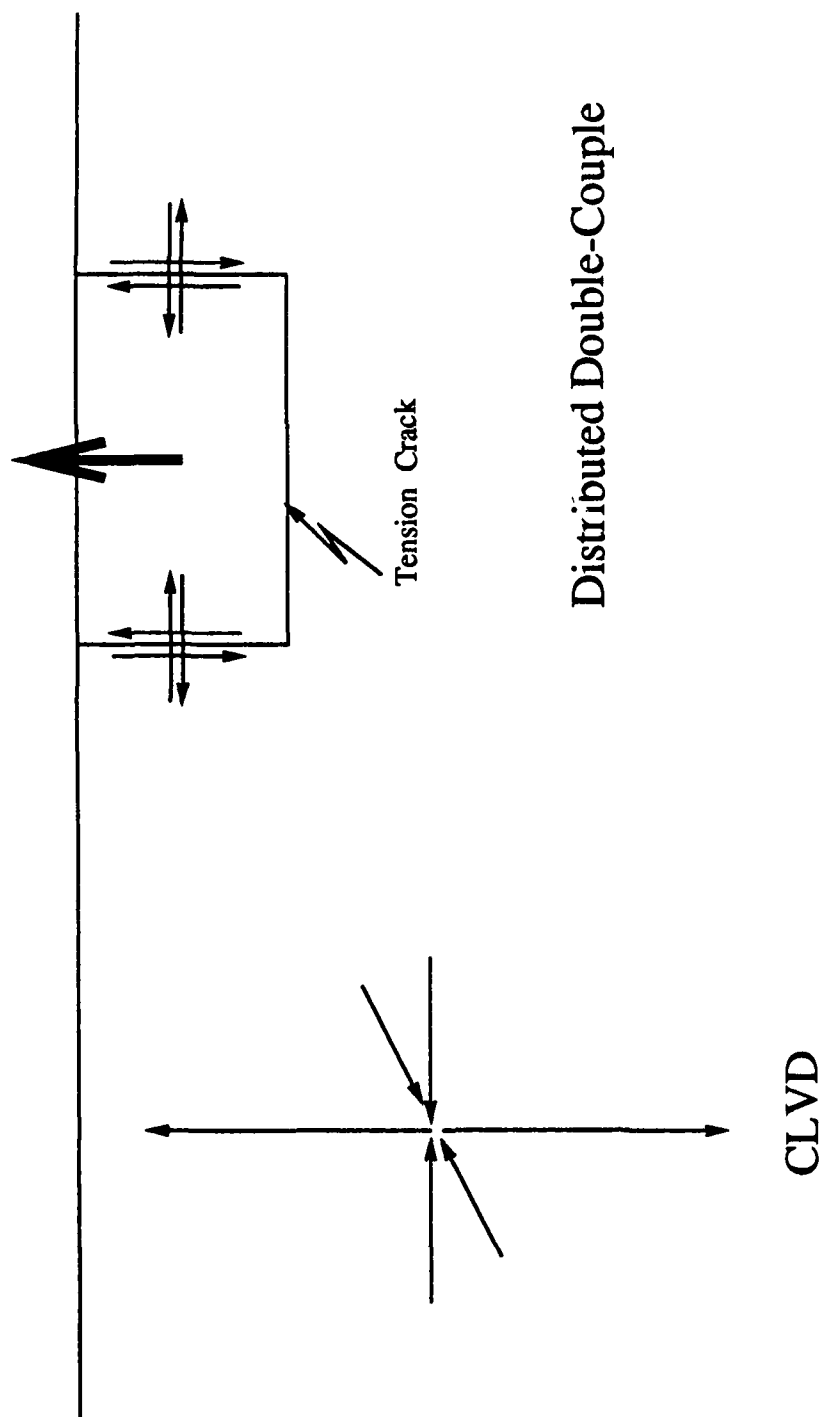


Figure 19. Comparison of the far-field SV-waves from the 2D-1D (solid lines) Shagan River simulations with the tension crack model (dashed lines) at three take-off angles for a depth of burial of 980 m.



Alternative SV Sources

Figure 20. Sketch of alternative sources of SV: the compensated linear vector dipole (left) and a distributed double-couple (right).

$$m = s(\xi_1, \xi_2, t) (\lambda + 2\mu) \begin{bmatrix} \frac{1}{2} & 0 & 0 \\ 0 & \frac{1}{2} & 0 \\ 0 & 0 & -1 \end{bmatrix}$$

This moment tensor has zero trace. Following the analysis in Section 2, the formulas for the displacements (P along the ray, SV normal to the ray) are similar to Equations (14) and (15),

$$u_{CLVD}^P = \frac{C^P}{R} F_{CLVD}^P(\omega, k) e^{-ik_{\alpha n} \hat{r}} \int_0^a S(\omega, r_0) r_0 dr_0 .$$

and

$$u_{CLVD}^{SV} = \frac{C^{SV}}{R} F_{CLVD}^{SV}(\omega, k) e^{-ik_{\beta n} \hat{r}} \int_0^a S(\omega, r_0) r_0 dr_0 ,$$

where

$$F_{CLVD}^P(\omega, k) = (\lambda + 2\mu) \left(\frac{1}{2} \Delta^{r_0} k - \partial_{z_0} \Delta^{z_0} \right) ,$$

$$F_{CLVD}^{SV}(\omega, k) = (\lambda + 2\mu) \left(\frac{1}{2} \omega^{r_0} k - \partial_{z_0} \omega^{z_0} \right) .$$

We then formed the sum

$$u = v u_{crack} + (1-v) u_{CLVD}$$

where u_{crack} is the tension crack solution, and $0 \leq v \leq 1$. We assumed the time and spatial dependence of $S(\omega, r_0)$ was the same for both the tension crack and CLVD. Figures 21 and 22 show the comparisons for the P and SV waves for the DOB=980 case with $v = 0$ (all CLVD, no tension crack), which we found works best for this DOB. We see that the P wave solutions are changed little except at the shallowest take-off angle (30°), where the second peak in the CLVD solutions is now too large. On the other hand, the comparisons for the SV waves are greatly improved. The shape and

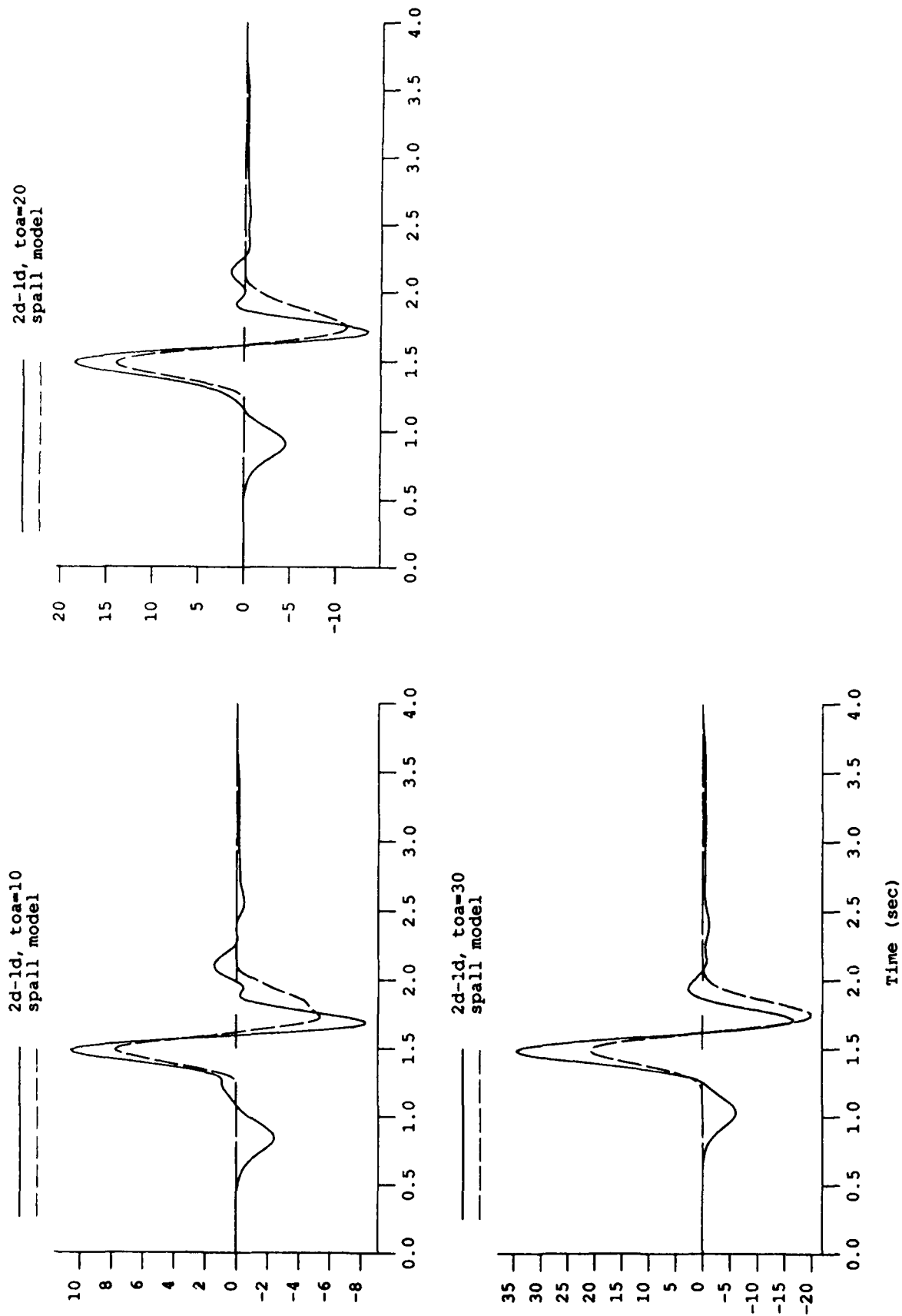


Figure 21. Comparison of the far-field SV-waves from the 2D-1D (solid lines) Shagan River simulations with the CLVD model (dashed lines) (with no tension crack contribution) at three take-off angles for a depth of burial of 980 m

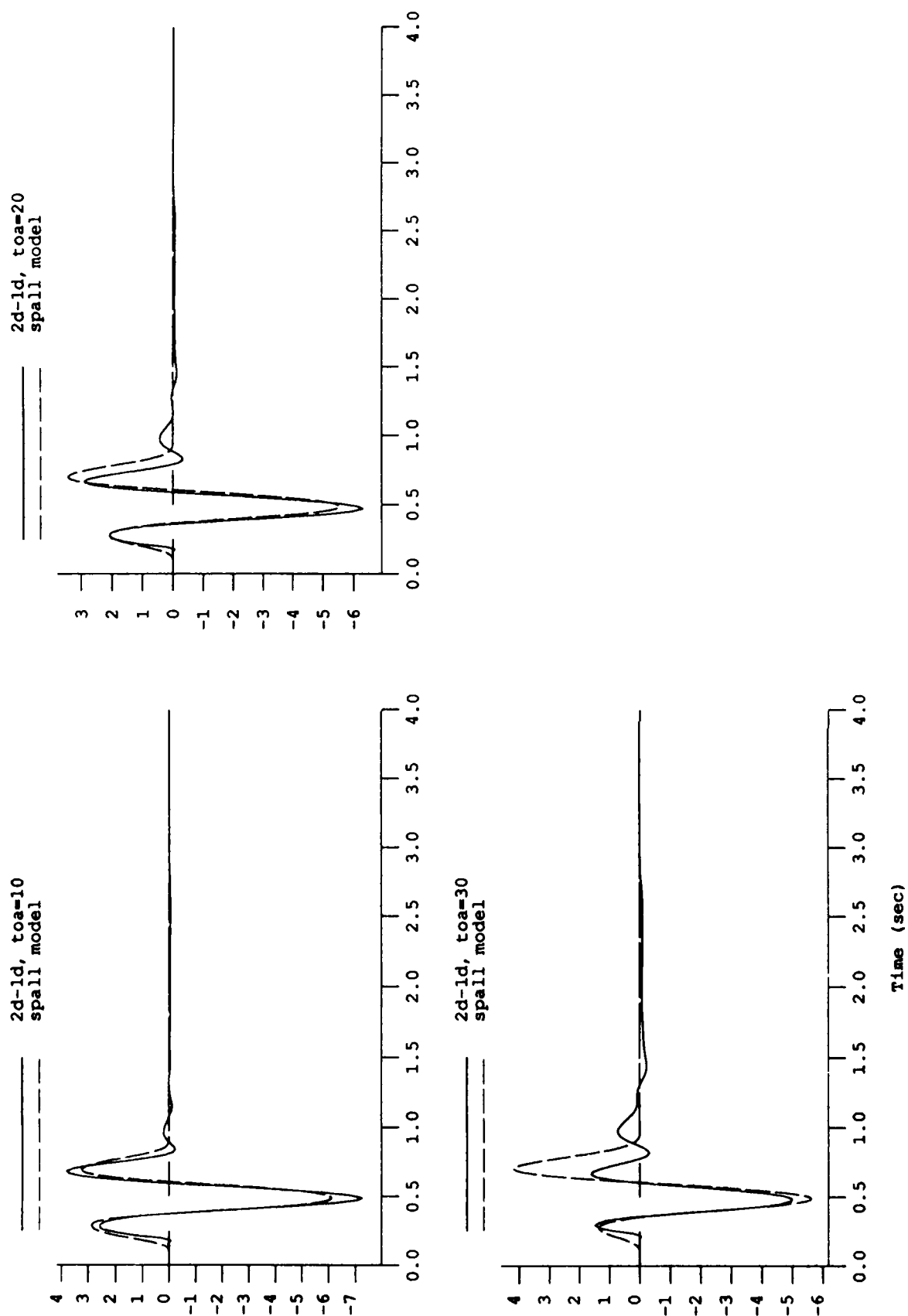


Figure 22. Comparison of the far-field P-waves from the 2D-1D (solid lines) Shagan River simulations with the CLVD model (dashed lines) (with no tension crack contribution) at three take-off angles for a depth of burial of 980 m

amplitudes agree fairly well. The initial negative part of the 2D-1D signals is a direct S wave from the explosive source. It is not part of the free surface interaction which we are modeling here. For the DOB=680 case, we found that a value of $\nu = 0.5$ (equal parts tension crack and CLVD) works better than other choices, but the results are not as good as for DOB=980, as can be seen in Figures 23 and 24. Although the amplitudes of the main peak are matched well, the apparent period and change with take-off angle of the following trough are matched poorly. We find that adding the CLVD source to the tension crack for the shallow DOB's (200 and 300) worsens the comparisons.

Since this approach showed some promise, we also hypothesized that additional sources of shear waves may be emanating from vertical cracks which are the boundaries of a cylinder which moves above the horizontal tension crack. That is, we imagine that the material above the tension crack moves up and down as a unit, shaped as a cylinder whose base is the tension crack. The relative motion along the vertical sides would act as a distributed shear dislocation. Without showing the details, we summarize by saying that after including this source in the computer code, its contribution to the DOB=680 and 980 SV solutions was too small to match the 2D-1D differences.

The tension crack model presented here matches the P waves due to free surface interactions in these simulations very well, but the model includes only part of the SV wave generation mechanisms.

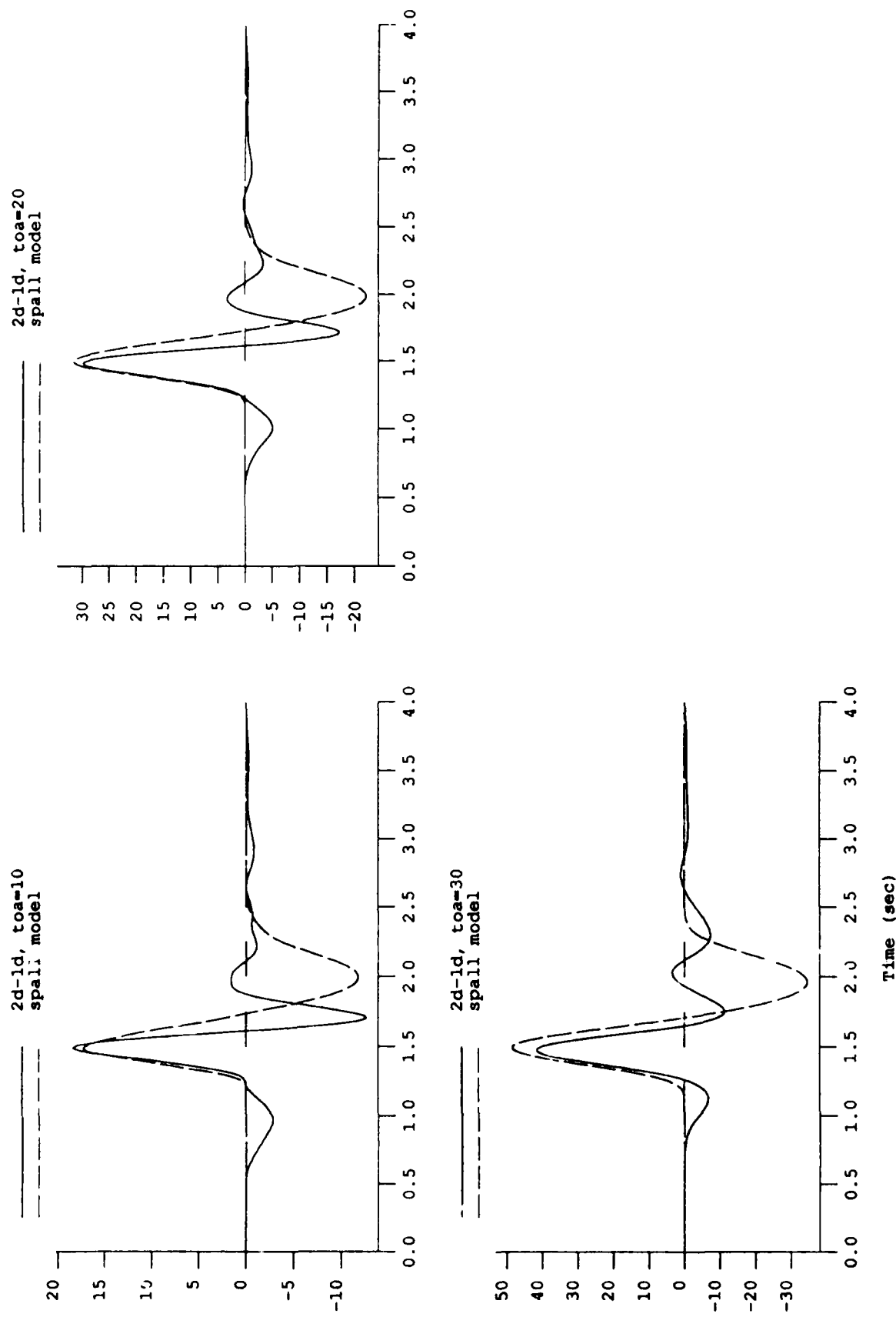


Figure 23. Comparison of 2D-1D far-field SV-waves (solid lines) and results using 1/2 CLVD and 1/2 tension crack contributions (dashed lines) at three take-off angles for a depth of burial of 680 m from the Shagan River simulations.

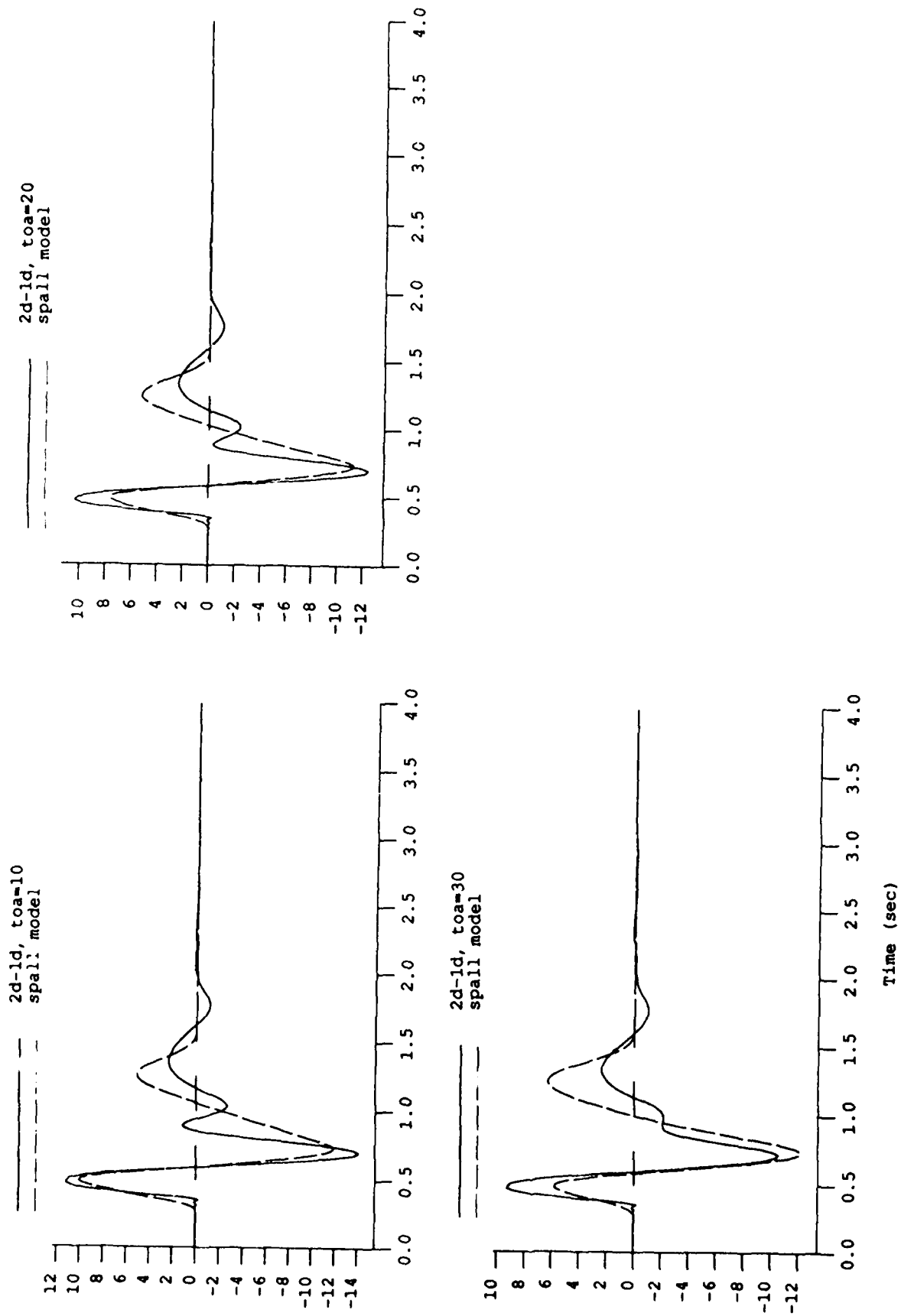


Figure 24. Comparison of 2D-1D far-field P-waves (solid lines) and results using 1/2 CLVD and 1/2 tension crack contributions (dashed lines) at three take-off angles for a depth of burial of 680 m from the Shagan River simulations.

3.2. Pahute Mesa Simulations

The 2D and 1D P-wave signals are overlain in Figures 25 through 27. The calculations were done at DOB's of 200, 680 and 980 m for the Pahute Mesa model, but not at 300 m. The take-off angles (3.3° , 11.4° , 16.7°) were chosen so that the phase velocities are the same as in the Shagan River simulations above. The first peaks of the 1D and 2D signals align closely. For DOB's 680 and 980, the apparent pP from the 2D waveforms is lagged about 0.2 seconds relative to the elastic pP in the 1D waveforms. The 2D pP amplitudes are attenuated relative to 1D amplitudes for the shallower take-off angles (11.4° and 16.7°).

As with the Shagan River simulations, we fit the tension crack model to the 2D-1D difference time series. The results are shown in the comparison plots in Figures 28 through 30. The fits of the model to the 2D-1D signals are generally good for the three DOB's and take-off angles. The parameters of the model are

Table 3.3 Spall Model Parameters for the Pahute Mesa Simulations				
Depth of Burial	Crack Depth	Crack Radius	Minimum Detachment Velocity	Maximum Detachment Velocity
z_{exp} (m)	z_s (m)	a (m)	v_1 (m/sec)	v_2 (m/sec)
200	150	400	1.1	22
680	200	2200	1.1	2
980	150	2200	1.1	2

There are several differences between the model parameters derived here and those for the Shagan River simulations. First, in the Shagan case, we found that the solutions were insensitive to the choice of the form of the source function $S(\omega, r_0)$. This is not

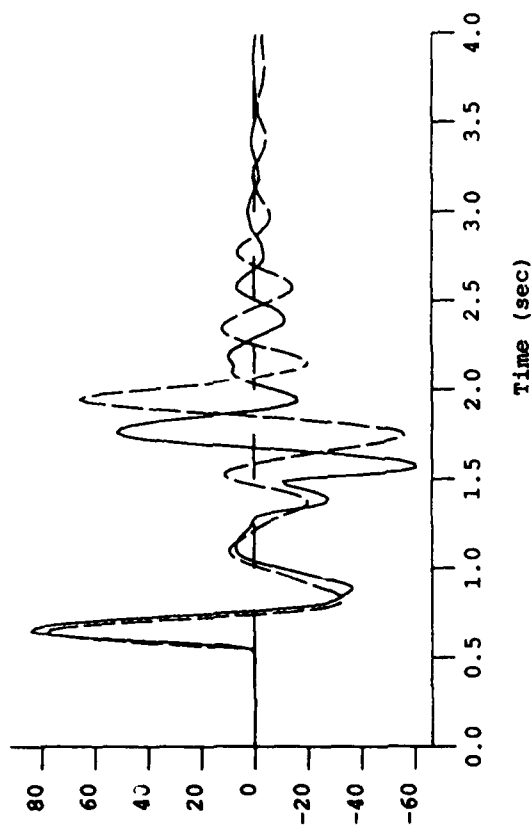
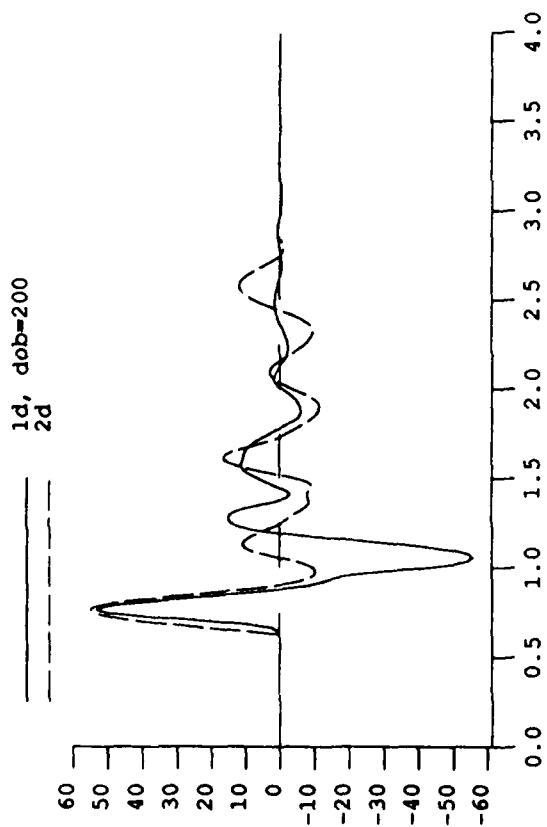
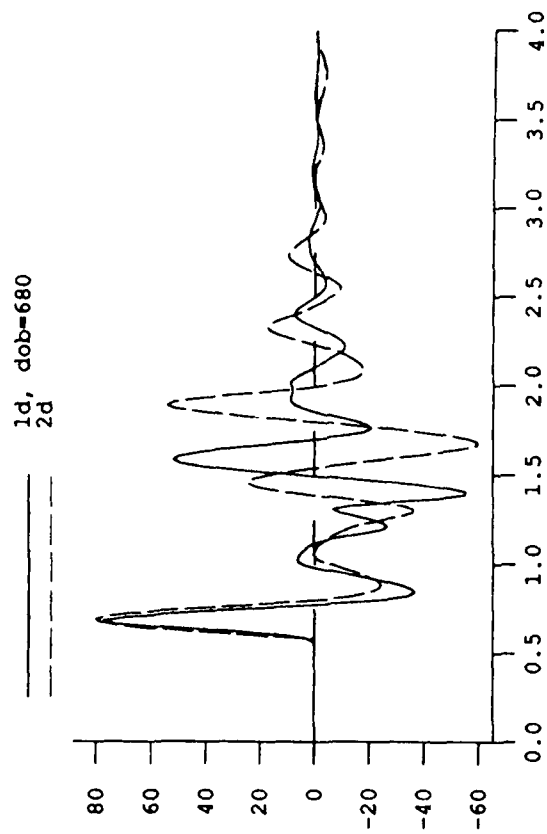
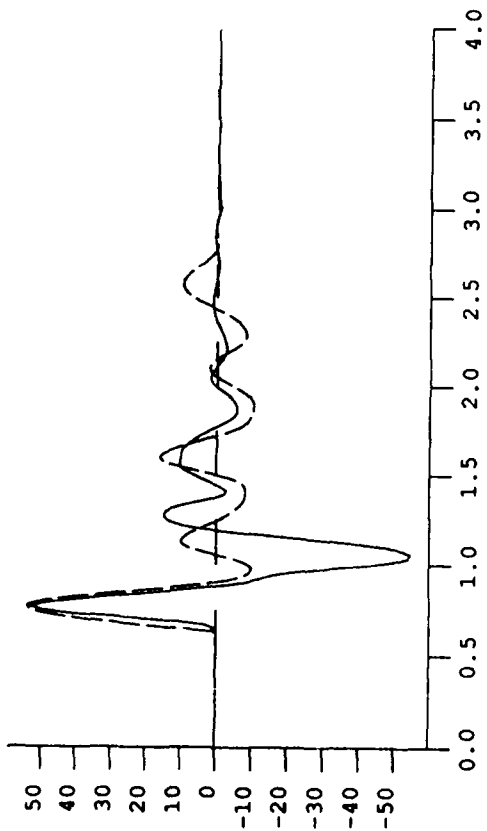
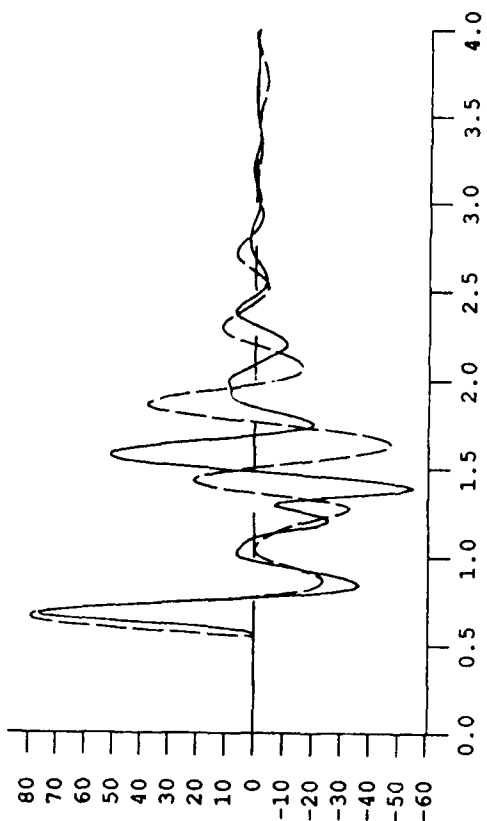


Figure 25. Comparison of the far-field P-waves from the 1D (solid lines) and 2D (dashed lines) Pahute Mesa simulations for three depths of burial at a take-off angle of 3.3° .

1d, dob=200
2d



1d, dob=680
2d



1d, dob=980
2d

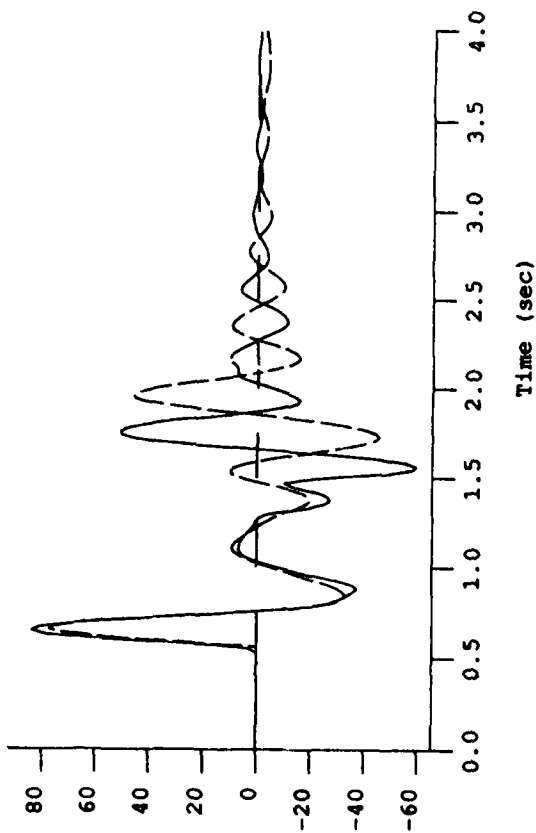


Figure 26. Comparison of the far-field P-waves from the 1D (solid lines) and 2D (dashed lines) Pahute Mesa simulations for three depths of burial at a take-off angle of 11.4° .

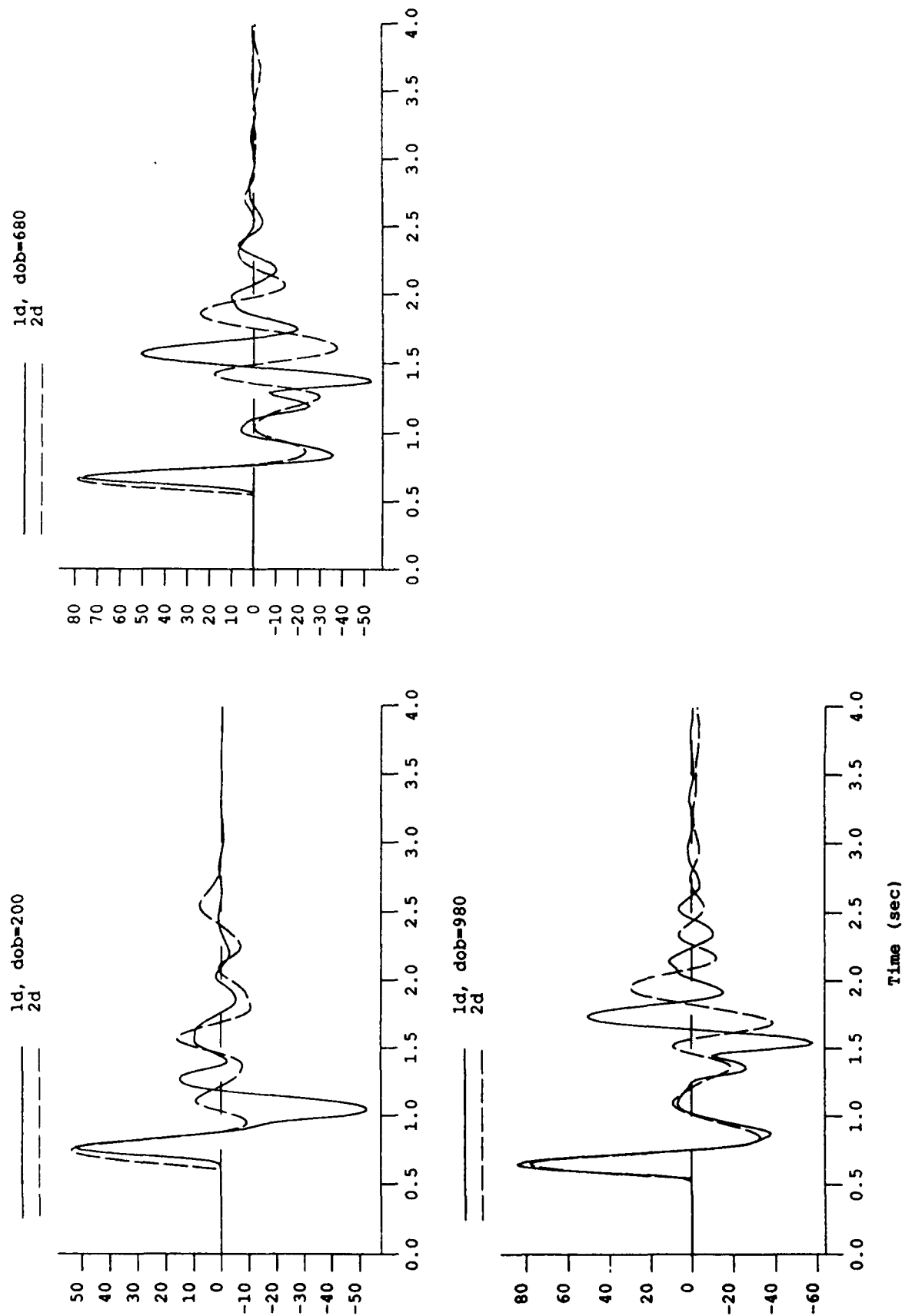
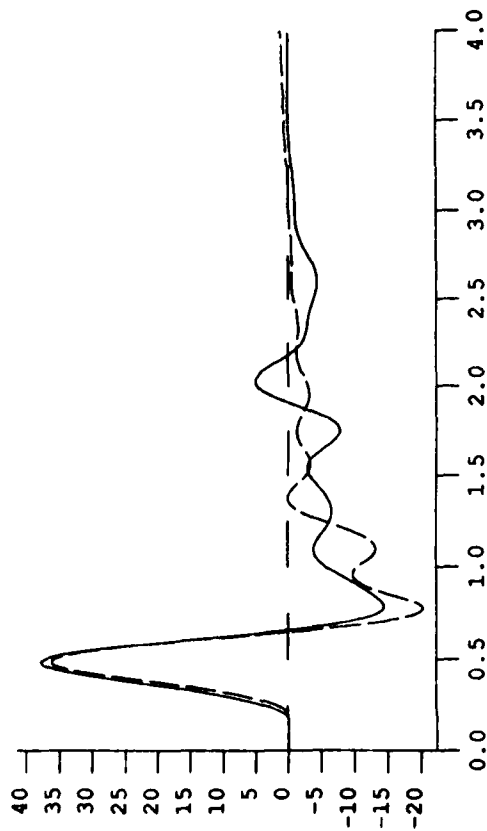
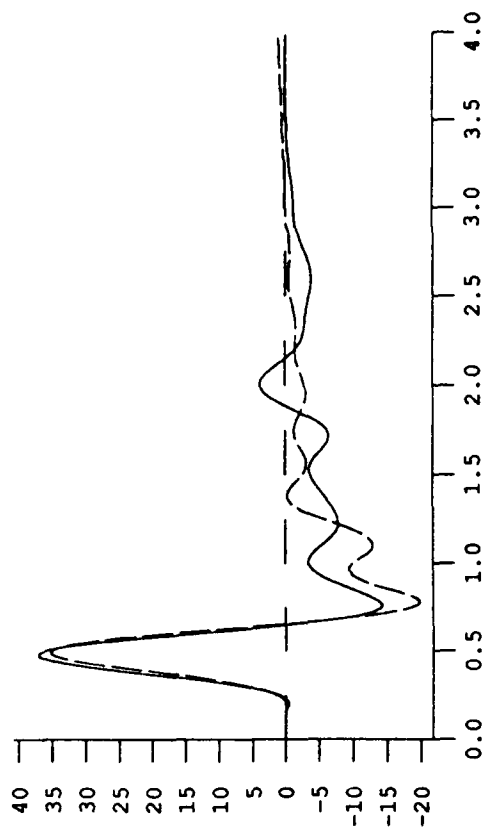


Figure 27. Comparison of the far-field P-waves from the 1D (solid lines) and 2D (dashed lines) Pahute Mesa simulations for three depths of burial at a take-off angle of 16.7°.

2d-1d, toa=3.3
spall model



2d-1d, toa=11.4
spall model



2d-1d, toa=16.7
spall model

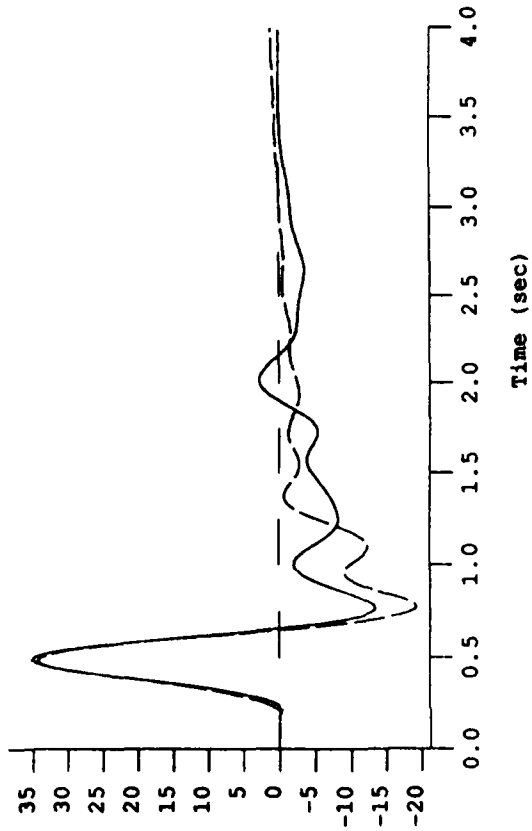


Figure 28. Comparison of the far-field P-waves from the 2D-1D (solid lines) Pahute Mesa simulations with the tension crack model (dashed lines) at three take-off angles for a depth of burial of 200 m.

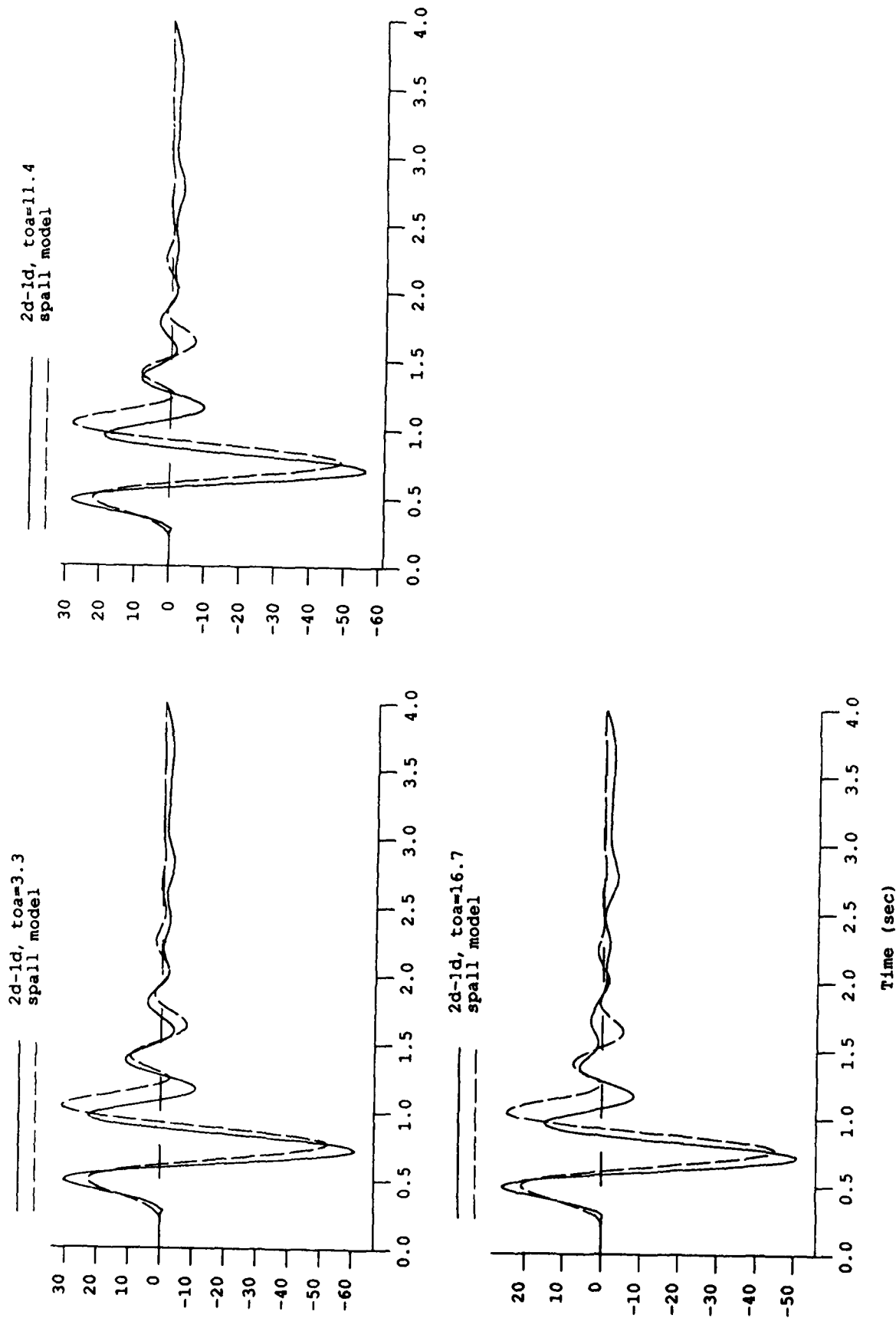


Figure 29. Comparison of the far-field P-waves from the 2D-1D (solid lines) Pahute Mesa simulations with the tension crack model (dashed lines) at three take-off angles for a depth of burial of 680 m.

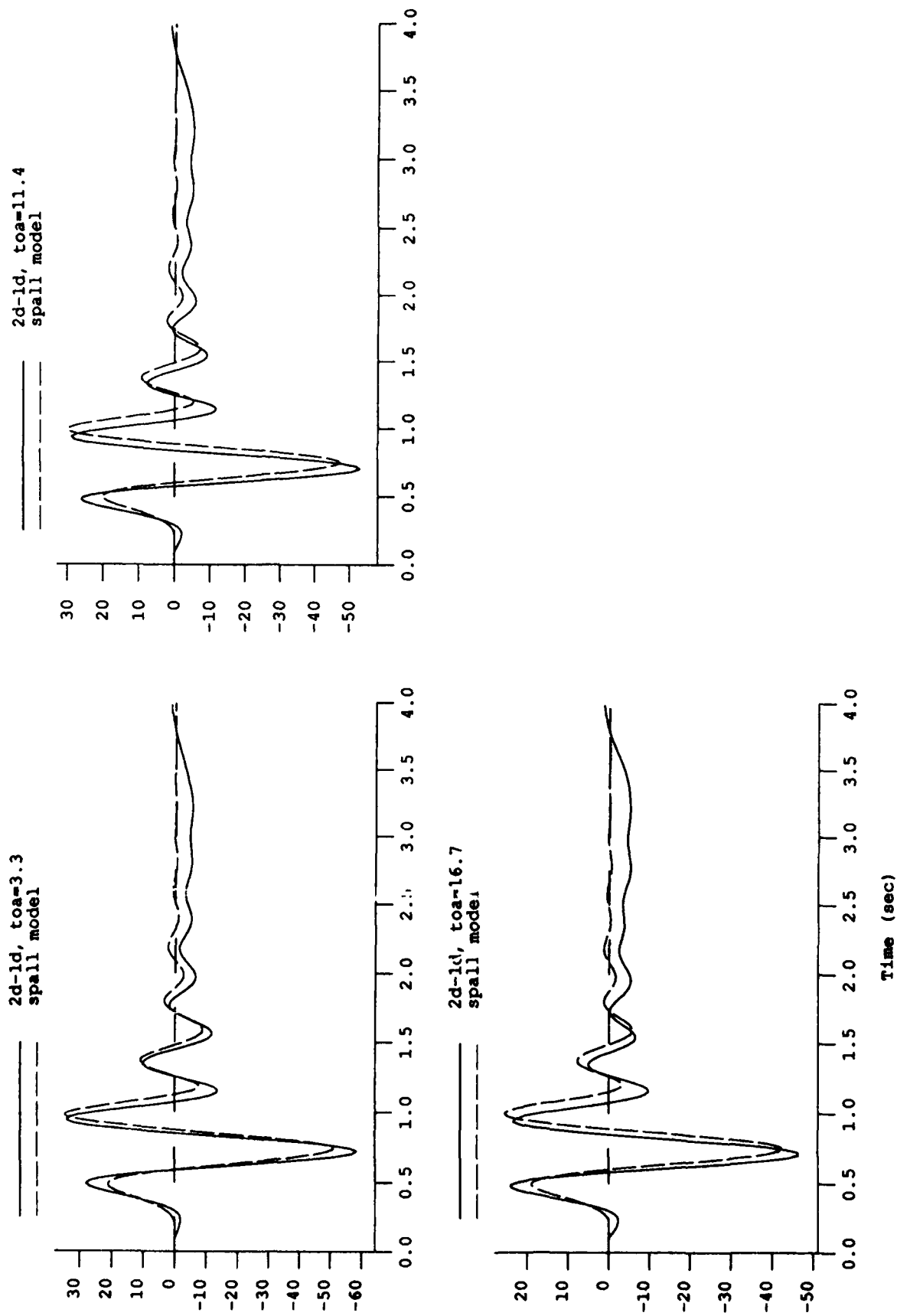


Figure 30. Comparison of the far-field P-waves from the 2D-1D (solid lines) Pahute Mesa simulations with the tension crack model (dashed lines) at three take-off angles for a depth of burial of 980 m.

the case for the Pahute Mesa runs, where we found that $S(\omega, r_0)$ must be distributed over the crack with the largest values near the center. This is due to the lower wave speeds, and hence phase velocities, in the Pahute Mesa model (Table 3.1). In Figures 28 through 30, a Gaussian spatial dependence with onset lagged by the pP time from the explosion (see Section 2.1 and 2.2) was used. The solutions were not sensitive to the details of the spatial dependence, as long as the maximum was at the center and went to zero at the edge. This spatial dependence was required to match the change in 2D-1D signals with take-off angle. It was not needed for the Shagan River runs because the wave speeds were about twice those for Pahute Mesa. For example, we show the tension crack signals for a constant $S(\omega, r_0)$ for DOB=980 with the 2D-1D signals in Figure 31. It can be seen that the results are not as good as in Figure 29 where the Gaussian spatial dependence was used.

Another feature of the Pahute Mesa simulations that differs from the Shagan River runs is the large change in crack radius between the case for DOB=200 and the other two DOB's. This is presumably due to the shallow layering in the Pahute Mesa earth model. Although the tension crack had a maximum detachment velocity (22 m/sec) similar to Shagan, it occurred over a much smaller radius (400 m).

A further difference between the models for the two sites is that the maximum detachment velocities for Pahute Mesa were the same for DOB's 680 and 980, whereas the velocity decreased from DOB=680 to 980 in the Shagan model. This is again attributed to differences in the shallow nonlinear properties.

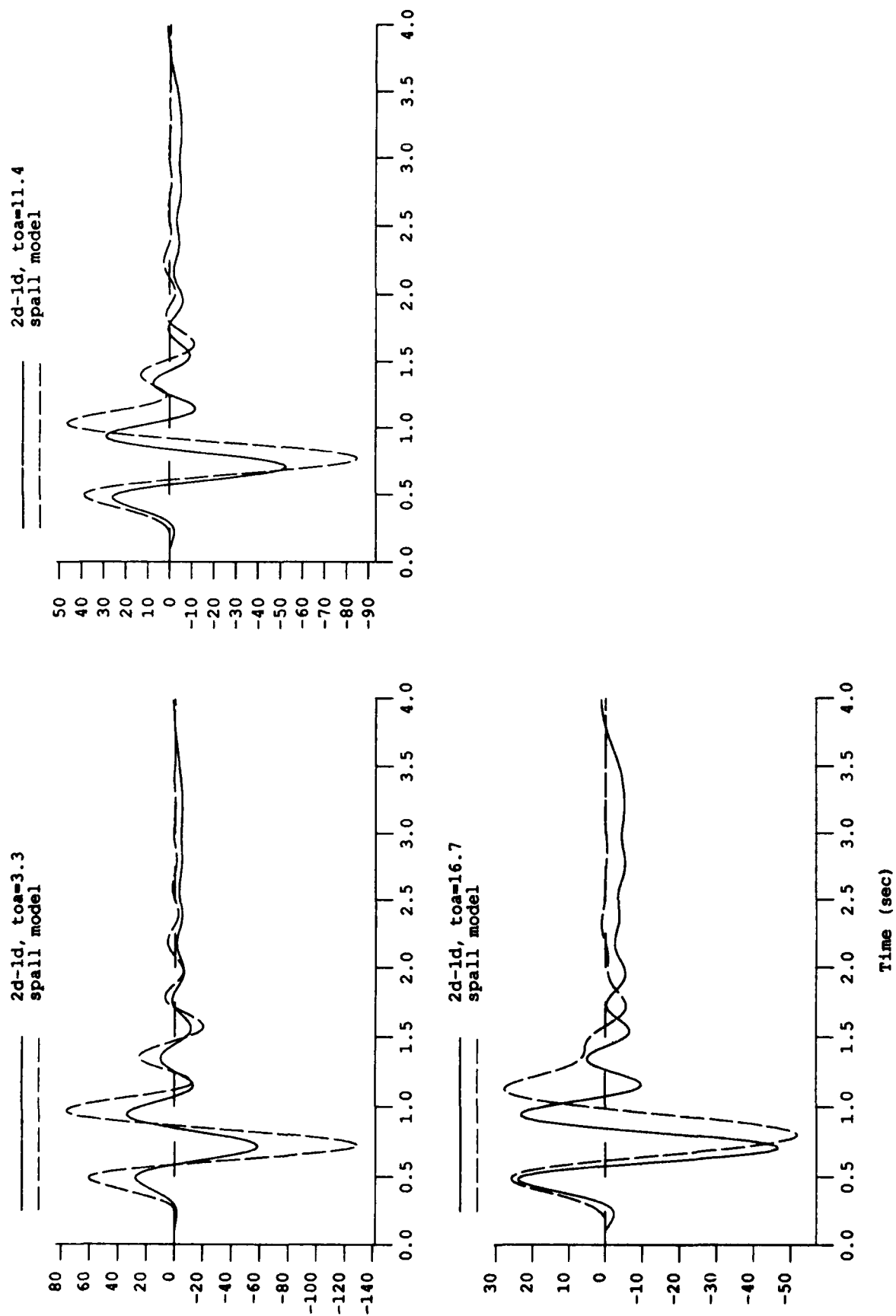


Figure 31. Comparison of the far-field P-waves from the 2D-1D (solid lines) Pahute Mesa simulations with the tension crack model with constant slip (dashed lines) at three take-off angles for a depth of burial of 980 m.

We computed the SV waves for the tension crack using the parameters in Table 3.3, and compared them to the 2D-1D difference waveforms. They are shown in Figure 32, for DOB=680 m. As with the Shagan River simulations, the 2D-1D signals are larger than those from the tension crack. Again this indicates that processes are generating SV waves in the simulations that are not included in the tension crack model.

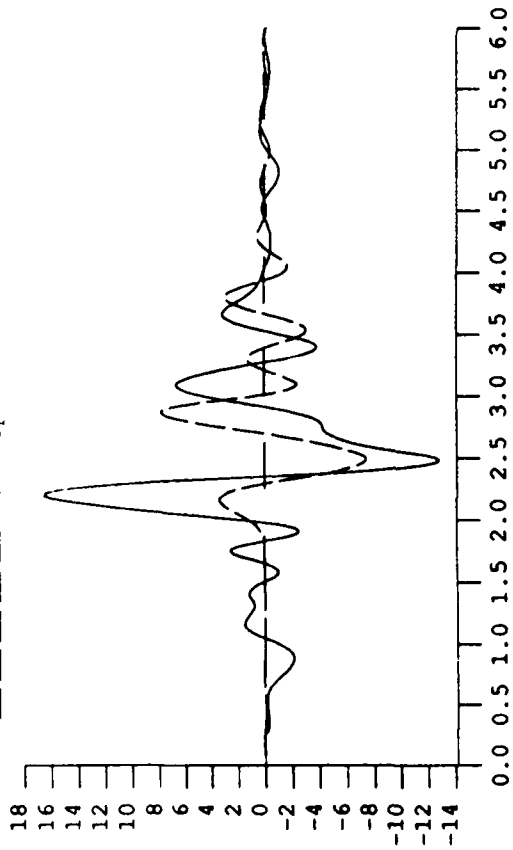
3.3. Comparisons with Observations

From observations of surface ground motions and of physical manifestations of Pahute Mesa tests, several authors have estimated the parameters of the spall process. In Table 3.4, we compare their results with those for the tension crack model at the optimal DOB (680).

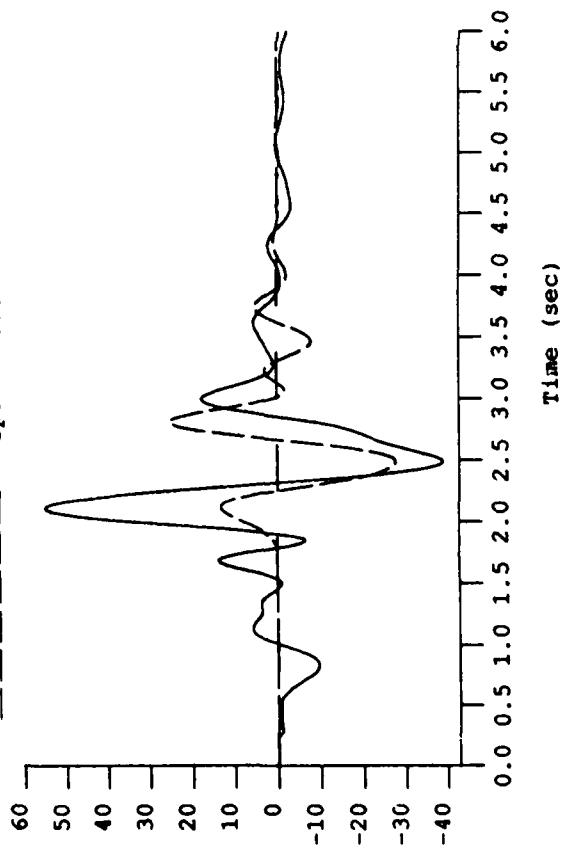
Table 3.4. Spall parameters from field observations and from the tension crack model for Pahute Mesa						
Parameter	Tension Crack	Patton (1990)	Sobel (1978)	Viecelli (1973)	Stump (1985)	Rawson (1988)
Maximum Velocity (m/sec)	2	6.4		8		
Radius (m)	2200	1750		500		500-2665
Momentum ($\times 10^{12}$ Nt-s)	7.5	9.2	3.5	0.58		
Mass ($\times 10^{12}$ Kg)	5.3	3.5	1.2	0.2	3.0	
Depth (m)	200			110		100-400

The authors cited in the table typically expressed their results as scaled values, in which case we used 125 KT, the yield in the simulations. In addition, the values in

2d-1d, toa=3.3
spall model



2d-1d, toa=16.7
spall model



2d-1d, toa=11.4
spall model

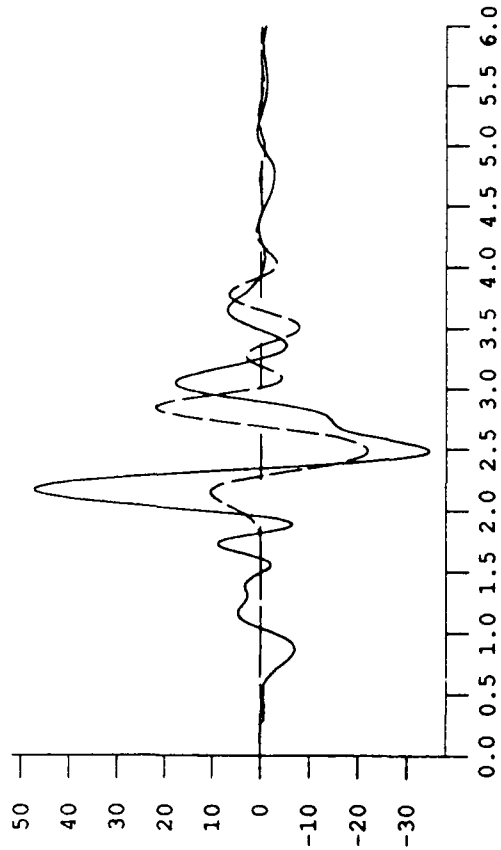


Figure 32. Comparison of the far-field SV-waves from the 2D-1D (solid lines) Pahute Mesa simulations with the tension crack model with Gaussian slip distribution (dashed lines) at three take-off angles for a depth of burial of 680 m.

Table 3.4 are the average values given by the authors. The mean detachment velocity (1.55 m/sec) was used to compute the tension crack momentum, rather than the maximum velocity. The momentum, spall radius and depth from the tension crack model lie within the spread of those inferred from observations. The mass is at the high end while the maximum velocity is at the low end.

It is very difficult to estimate the parameters in Table 3.4 because of a paucity of direct observations. There are typically few surface ground motion sensors, and no sub-surface observations of ground motion or other phenomena such as cracking. Inference of the spall process beyond estimating apparent pP amplitude and travel time from far-field recordings has not been successful. With these limitations in mind, it can be said that the parameters of this study are consistent with published field observations.

4. SUMMARY AND CONCLUSIONS

We show that a simple model can be constructed which generates the far-field P waves of a two-dimensional nonlinear calculation which includes the effects of the free-surface for a range of depths-of-burial. The model which fits the P-waves from the Shagan River simulations underestimates the SV-waves. The model, proposed in its original form by Day, *et al.* (1983), is based on using a tension crack which opens due to the tension wave from the free surface. The material over the crack travels up with the impulse of the tension wave and returns under the influence of gravity. Stump (1985) modified the original model to include the effects of source by adding an empirical time function based on chemical explosions. The modified model was used by Taylor and Randall (1989) to model regional seismograms. In our formalism presented in this report, we include the effects of source finiteness and those of crustal reverberations. A time dependence is a natural consequence.

The parameters of the model compare favorably with observations based on field data. In addition, McLaughlin, *et al.* (1990), use the model to compute regional seismograms and find that in the Lg bandwidth, the spall contribution should be comparable to or greater than that of the explosion signal alone. Since the spall model which fits the P-waves in our study generates SV-waves that are too small, the spall model may lead to an underestimate of the Lg from spall. Spall, therefore, appears to be a very significant source of Lg.

5. REFERENCES

- Aki, K, P. G. Richards (1980). *Quantitative Seismology, Theory and Methods, Volume I*, Freeman, San Francisco, 556 pages.
- Bache, T. C. and D. G. Harkrider (1976). The Body Waves Due to a General Seismic Source in a Layered Earth Model: 1. Formulation of the Theory, *Bull. Seism. Soc. Am.*, **66** (6), 1805-1819.
- Bache, T. C., S. M. Day and H. J. Swanger (1982). Rayleigh Wave Synthetic Seismograms from Multi-Dimensional Simulations of Underground Explosions, *Bull. Seism. Soc. Am.*, **54**, 1875-1888.
- Day, S. M, N. Rimer, and J. T. Cherry (1983). Surface Waves from Underground Explosions with Spall: Analysis of Elastic and Nonlinear Source Models, *Bull. Seism. Soc. Am.* **73**, 247-264.
- Day, S. M., N. Rimer, T. G. Barker, E. J. Halda, and B. Shkoller (1986). Numerical Study of Depth of Burial Effects on the Seismic Signature of Underground Explosions, S-CUBED Technical Report to Defense Nuclear Agency DNA-TR-86-114.
- Eisler, J. D. and F. Chilton (1964). Spalling of the Earth's Surface by Underground Nuclear Explosions, *J. Geophys. Res.*, **69**, 5285-5293.
- Fuchs, K. (1966). The Transfer Function for P-Waves for a System Consisting of a Point Source in a Layered Medium, *Bull. Seism. Soc. Am.*, **56** (10), 75-108.
- Knopoff, L. and M. J. Randall (1970). The Compensated Lienar-Vector Dipole: A Possible Mechanism for Earthquakes, *J. Geophy. Res.*, **75** (26), 4957-4963.
- McLaughlin, K. L., T. G. Barker, S. M. Day, B. Shkoller, and J. L. Stevens (1988). Effects of Depth of Burial and Tectonic Release on Regional and Teleseismic Explosion Waveforms AFGL-TR-88-0314, S-CUBED Report SSS-R-88-9844. ADA207541
- McLaughlin, K.L., T. G. Barker, S. M. Day (1990). Implications of Explosion Generated Spall Models: Regional Seismic Signals, S-CUBED Scientific Report No. 2 to AFGL, GL-TR-90-0133, SSS-TR-90-11535. ADA227273
- Murphy, J. R., and T. J. Bennett (1983). A Discrimination Analysis of Short-Period Regional Seismic Data at Tonto Forest Observatory, *Bull. Seism. Soc. Am.*, **72**, 1351-1366.
- Patton, H. J. (1990). Estimates of Spall Mass and Spall Impulse from Observed Strong Ground Motions on Pahute Mesa, submitted to *Bull. Seism. Soc. Am.*
- Rawson, G. (1988), How *In-Situ* Stress, Induced Stress, Fracturing and Spall Might Affect Critical Depths for Explosion Containment and Cratering. Lawrence Livermore National Laboratory Report No. UCID-890398.

- Rodi, W. L., J. M. Savino, T. G. Barker, S. M. Day and T. C. Bache (1978). Analysis of Explosion Generated Surface Waves in Africa, Results from the Discrimination Experiment and Summary of Current Research. Systems, Science and Software Quarterly Technical Report, SSS-R-78-3653.
- Sobel, P. A. (1978). The Effect of Spall on mb and Ms, Teledyne Geotech Report, SDAC-TR-77-12, Dallas, TX.
- Stump, B. W. (1984). Resolving Point and Couples Forces in Explosion Modeling (Abstract), *EOS*, **65**, 995.
- Stump, B. W. (1985). Constraints on Explosive Sources with Spall from Near-Source Waveforms, *Bull. Seism. Soc. Am.*, **75**, 361-378.
- Taylor, S. R., N. W. Sherman, and M. D. Denny, Spectral Discrimination Between NTS Explosions and Western Unites States Earthquakes at Regional Distances, *Bull. Seism. Soc. Am.*, **78**, 1563-1579.
- Taylor, S. R. and G.E. Randall (1989). The Effects of Spall on Regional Seismograms, *Geophys. Res. Lett.*, **16**, 211-214.
- Viecelli, J. A. (1973). Spallation and the Generation of Surface Waves by an Underground Explosion, *J. Geophys. Res.*, **78**, 2475-2487.

CONTRACTORS (UNITED STATES)

Prof. Thomas Ahrens
Seismological Lab, 252-21
Division of Geological & Planetary Sciences
California Institute of Technology
Pasadena, CA 91125

Prof. Charles B. Archambeau
CIRES
University of Colorado
Boulder, CO 80309

Dr. Thomas C. Bache, Jr.
Science Applications Int'l Corp.
10260 Campus Point Drive
San Diego, CA 92121 (2 copies)

Prof. Muawia Barazangi
Institute for the Study of the Continent
Cornell University
Ithaca, NY 14853

Dr. Douglas R. Baumgardt
ENSCO, Inc
5400 Port Royal Road
Springfield, VA 22151-2388

Prof. Jonathan Berger
IGPP, A-025
Scripps Institution of Oceanography
University of California, San Diego
La Jolla, CA 92093

Dr. Lawrence J. Burdick
Woodward-Clyde Consultants
566 El Dorado Street
Pasadena, CA 91109-3245

Dr. Jerry Carter
Center for Seismic Studies
1300 North 17th St., Suite 1450
Arlington, VA 22209-2308

Dr. Karl Coyner
New England Research, Inc.
76 Olcott Drive
White River Junction, VT 05001

Prof. Vernon F. Cormier
Department of Geology & Geophysics
U-45, Room 20/
The University of Connecticut
Storrs, CT 06268

Professor Anton W. Dainty
Earth Resources Laboratory
Massachusetts Institute of Technology
42 Carleton Street
Cambridge, MA 02142

Prof. Steven Day
Department of Geological Sciences
San Diego State University
San Diego, CA 92182

Dr. Zoltan A. Der
ENSCO, Inc.
5400 Port Royal Road
Springfield, VA 22151-2388

Prof. John Ferguson
Center for Lithospheric Studies
The University of Texas at Dallas
P.O. Box 830688
Richardson, TX 75083-0688

Prof. Stanley Flatte
Applied Sciences Building
University of California
Santa Cruz, CA 95064

Dr. Alexander Florence
SRI International
333 Ravenswood Avenue
Menlo Park, CA 94025-3493

Prof. Stephen Grand
University of Texas at Austin
Department of Geological Sciences
Austin, TX 78713-7909

Prof. Henry L. Gray
Vice Provost and Dean
Department of Statistical Sciences
Southern Methodist University
Dallas, TX 75275

Dr. Indra Gupta
Teledyne Geotech
314 Montgomery Street
Alexandria, VA 22314

Prof. David G. Harkrider
Seismological Laboratory
Division of Geological & Planetary Sciences
California Institute of Technology
Pasadena, CA 91125

Prof. Donald V. Helmberger
Seismological Laboratory
Division of Geological & Planetary Sciences
California Institute of Technology
Pasadena, CA 91125

Prof. Eugene Herrin
Institute for the Study of Earth and Man
Geophysical Laboratory
Southern Methodist University
Dallas, TX 75275

Prof. Robert B. Herrmann
Department of Earth & Atmospheric Sciences
St. Louis University
St. Louis, MO 63156

Prof. Bryan Isacks
Cornell University
Department of Geological Sciences
SNEE Hall
Ithaca, NY 14850

Dr. Rong-Song Jih
Teledyne Geotech
314 Montgomery Street
Alexandria, VA 22314

Prof. Lane R. Johnson
Seismographic Station
University of California
Berkeley, CA 94720

Prof. Alan Kafka
Department of Geology & Geophysics
Boston College
Chestnut Hill, MA 02167

Dr. Richard LaCoss
MIT-Lincoln Laboratory
M-200B
P. O. Box 73
Lexington, MA 02173-0073 (3 copies)

Prof. Fred K. Lamb
University of Illinois at Urbana-Champaign
Department of Physics
1110 West Green Street
Urbana, IL 61801

Prof. Charles A. Langston
Geosciences Department
403 Deike Building
The Pennsylvania State University
University Park, PA 16802

Prof. Thorne Lay
Institute of Tectonics
Earth Science Board
University of California, Santa Cruz
Santa Cruz, CA 95064

Prof. Arthur Lerner-Lam
Lamont-Doherty Geological Observatory
of Columbia University
Palisades, NY 10964

Dr. Christopher Lynnes
Teledyne Geotech
314 Montgomery Street
Alexandria, VA 22314

Prof. Peter Malin
University of California at Santa Barbara
Institute for Crustal Studies
Santa Barbara, CA 93106

Dr. Randolph Martin, III
New England Research, Inc.
76 Olcott Drive
White River Junction, VT 05001

Dr. G. McCartor
Southern Methodist University
Dept of Physics
Dallas, TX 75275

Prof. Thomas V. McEvelly
Seismographic Station
University of California
Berkeley, CA 94720

Dr. Keith L. McLaughlin
S-CUBED
A Division of Maxwell Laboratory
P.O. Box 1620
La Jolla, CA 92038-1620

Prof. William Menke
Lamont-Doherty Geological Observatory
of Columbia University
Palisades, NY 10964

Stephen Miller
SRI International
333 Ravenswood Avenue
Box AF 116
Menlo Park, CA 94025-3493

Prof. Bernard Minster
IGPP, A-025
Scripps Institute of Oceanography
University of California, San Diego
La Jolla, CA 92093

Prof. Brian J. Mitchell
Department of Earth & Atmospheric Sciences
St. Louis University
St. Louis, MO 63156

Mr. Jack Murphy
S-CUBED, A Division of Maxwell Laboratory
11800 Sunrise Valley Drive
Suite 1212
Reston, VA 22091 (2 copies)

Dr. Bao Nguyen
GL/LWH
Hanscom AFB, MA 01731-5000

Prof. John A. Orcutt
IGPP, A-025
Scripps Institute of Oceanography
University of California, San Diego
La Jolla, CA 92093

Prof. Keith Priestley
University of Cambridge
Bullard Labs, Dept. of Earth Sciences
Madingley Rise, Madingley Rd.
Cambridge CB3 0EZ, ENGLAND

Prof. Paul G. Richards
Lamont Doherty Geological Observatory
of Columbia University
Palisades, NY 10964

Dr. Wilmer Rivers
Teledyne Geotech
314 Montgomery Street
Alexandria, VA 22314

Prof. Charles G. Sammis
Center for Earth Sciences
University of Southern California
University Park
Los Angeles, CA 90089-0741

Prof. Christopher H. Scholz
Lamont-Doherty Geological Observatory
of Columbia University
Palisades, NY 10964

Thomas J. Sereno, Jr.
Science Application Int'l Corp.
10260 Campus Point Drive
San Diego, CA 92121

Prof. David G. Simpson
Lamont-Doherty Geological Observatory
of Columbia University
Palisades, NY 10964

Dr. Jeffrey Stevens
S-CUBED
A Division of Maxwell Laboratory
P.O. Box 1620
La Jolla, CA 92038-1620

Prof. Brian Stump
Institute for the Study of Earth & Man
Geophysical Laboratory
Southern Methodist University
Dallas, TX 75275

Prof. Jeremiah Sullivan
University of Illinois at Urbana-Champaign
Department of Physics
1110 West Green Street
Urbana, IL 61801

Prof. Clifford Thurber
University of Wisconsin-Madison
Department of Geology & Geophysics
1215 West Dayton Street
Madison, WI 53706

Prof. M. Nafi Toksoz
Earth Resources Lab
Massachusetts Institute of Technology
42 Carleton Street
Cambridge, MA 02142

Prof. John E. Vidale
University of California at Santa Cruz
Seismological Laboratory
Santa Cruz, CA 95064

Prof. Terry C. Wallace
Department of Geosciences
Building #77
University of Arizona
Tucson, AZ 85721

Dr. Raymond Willeman
GL/LWH
Hanscom AFB, MA 01731-5000

Dr. Lorraine Wolf
GL/LWH
Hanscom AFB, MA 01731-5000

OTHERS (United States)

Dr. Monem Abdel-Gawad
Rockwell International Science Center
1049 Camino Dos Rios
Thousand Oaks, CA 91360

Prof. Keiiti Aki
Center for Earth Sciences
University of Southern California
University Park
Los Angeles, CA 90089-0741

Prof. Shelton S. Alexander
Geosciences Department
403 Deike Building
The Pennsylvania State University
University Park, PA 16802

Dr. Kenneth Anderson
BBNSTC
Mail Stop 14/1B
Cambridge, MA 02238

Dr. Ralph Archuleta
Department of Geological Sciences
University of California at Santa Barbara
Santa Barbara, CA 93102

Dr. Jeff Barker
Department of Geological Sciences
State University of New York
at Binghamton
Vestal, NY 13901

Dr. Susan Beck
Department of Geosciences, Bldg # 77
University of Arizona
Tucson, AZ 85721

Dr. T.J. Bennett
S-CUBED
A Division of Maxwell Laboratory
11800 Sunrise Valley Drive, Suite 1212
Reston, VA 22091

Mr. William J. Best
907 Westwood Drive
Vienna, VA 22180

Dr. N. Biswas
Geophysical Institute
University of Alaska
Fairbanks, AK 99701

Dr. G.A. Bollinger
Department of Geological Sciences
Virginia Polytechnic Institute
21044 Derring Hall
Blacksburg, VA 24061

Dr. Stephen Bratt
Center for Seismic Studies
1300 North 17th Street
Suite 1450
Arlington, VA 22209

Michael Browne
Teledyne Geotech
3401 Shiloh Road
Garland, TX 75041

Mr. Roy Burger
1221 Serry Road
Schenectady, NY 12309

Dr. Robert Burrige
Schlumberger-Doll Research Center
Old Quarry Road
Ridgefield, CT 06877

Dr. W. Winston Chan
Teledyne Geotech
314 Montgomery Street
Alexandria, VA 22314-1581

Dr. Theodore Cherry
Science Horizons, Inc.
710 Encinitas Blvd., Suite 200
Encinitas, CA 92024 (2 copies)

Prof. Jon F. Claerbout
Department of Geophysics
Stanford University
Stanford, CA 94305

Prof. Robert W. Clayton
Seismological Laboratory
Division of Geological & Planetary Sciences
California Institute of Technology
Pasadena, CA 91125

Prof. F. A. Dahlen
Geological and Geophysical Sciences
Princeton University
Princeton, NJ 08544-0636

Prof. Adam Dziewonski
Hoffman Laboratory
Harvard University
20 Oxford St
Cambridge, MA 02138

Prof. John Ebel
Department of Geology & Geophysics
Boston College
Chestnut Hill, MA 02167

Eric Fielding
SNEE Hall
INSTOC
Cornell University
Ithaca, NY 14853

Prof. Donald Forsyth
Department of Geological Sciences
Brown University
Providence, RI 02912

Dr. Cliff Frolich
Institute of Geophysics
8701 North Mopac
Austin, TX 78759

Dr. Anthony Gangi
Texas A&M University
Department of Geophysics
College Station, TX 77843

Dr. Freeman Gilbert
IGPP, A-025
Scripps Institute of Oceanography
University of California
La Jolla, CA 92093

Mr. Edward Giller
Pacific Sierra Research Corp.
1401 Wilson Boulevard
Arlington, VA 22209

Dr. Jeffrey W. Given
SAIC
10260 Campus Point Drive
San Diego, CA 92121

Prof. Roy Greenfield
Geosciences Department
403 Deike Building
The Pennsylvania State University
University Park, PA 16802

Dan N. Hagedorn
Battelle
Pacific Northwest Laboratories
Battelle Boulevard
Richland, WA 99352

Kevin Hutchenson
Department of Earth Sciences
St. Louis University
3507 Laclede
St. Louis, MO 63103

Dr. Hans Israelsson
Center for Seismic Studies
1300 N. 17th Street, Suite 1450
Arlington, VA 22209-2308

Prof. Thomas H. Jordan
Department of Earth, Atmospheric
and Planetary Sciences
Massachusetts Institute of Technology
Cambridge, MA 02139

Robert C. Kemerait
ENSCO, Inc.
445 Pineda Court
Melbourne, FL 32940

William Kikendall
Teledyne Geotech
3401 Shiloh Road
Garland, TX 75041

Prof. Leon Knopoff
University of California
Institute of Geophysics & Planetary Physics
Los Angeles, CA 90024

Prof. L. Timothy Long
School of Geophysical Sciences
Georgia Institute of Technology
Atlanta, GA 30332

Prof. Art McGarr
Mail Stop 977
Geological Survey
345 Middlefield Rd.
Menlo Park, CA 94025

Dr. George Mellman
Sierra Geophysics
11255 Kirkland Way
Kirkland, WA 98033

Prof. John Nabelek
College of Oceanography
Oregon State University
Corvallis, OR 97331

Dr. Susan Schwartz
Institute of Tectonics
1156 High St.
Santa Cruz, CA 95064

Prof. Geza Nagy
University of California, San Diego
Department of Ames, M.S. B-010
La Jolla, CA 92093

John Sherwin
Teledyne Geotech
3401 Shiloh Road
Garland, TX 75041

Prof. Amos Nur
Department of Geophysics
Stanford University
Stanford, CA 94305

Dr. Matthew Sibol
Virginia Tech
Seismological Observatory
4044 Derring Hall
Blacksburg, VA 24061-0420

Prof. Jack Oliver
Department of Geology
Cornell University
Ithaca, NY 14850

Prof. Robert Smith
Department of Geophysics
University of Utah
1400 East 2nd South
Salt Lake City, UT 84112

Prof. Robert Phinney
Geological & Geophysical Sciences
Princeton University
Princeton, NJ 08544-0636

Dr. Stewart W. Smith
Geophysics AK-50
University of Washington
Seattle, WA 98195

Dr. Paul Pomeroy
Rondout Associates
P.O. Box 224
Stone Ridge, NY 12484

Dr. George Sutton
Rondout Associates
P.O. Box 224
Stone Ridge, NY 12484

Dr. Jay Pulli
RADIX System, Inc.
2 Taft Court, Suite 203
Rockville, MD 20850

Prof. L. Sykes
Lamont-Doherty Geological Observatory
of Columbia University
Palisades, NY 10964

Dr. Norton Rimer
S-CUBED
A Division of Maxwell Laboratory
P.O. Box 1620
La Jolla, CA 92038-1620

Prof. Pradeep Talwani
Department of Geological Sciences
University of South Carolina
Columbia, SC 29208

Prof. Larry J. Ruff
Department of Geological Sciences
1006 C.C. Little Building
University of Michigan
Ann Arbor, MI 48109-1063

Prof. Ta-liang Teng
Center for Earth Sciences
University of Southern California
University Park
Los Angeles, CA 90089-0741

Dr. Richard Sailor
TASC Inc.
55 Walkers Brook Drive
Reading, MA 01867

Dr. R.B. Tittmann
Rockwell International Science Center
1049 Camino Dos Rios
P.O. Box 1085
Thousand Oaks, CA 91360

Dr. Gregory van der Vink
IRIS, Inc.
1616 North Fort Myer Drive
Suite 1440
Arlington, VA 22209

Professor Daniel Walker
University of Hawaii
Institute of Geophysics
Honolulu, HI 96822

William R. Walter
Seismological Laboratory
University of Nevada
Reno, NV 89557

Dr. Gregory Wojcik
Weidlinger Associates
4410 El Camino Real
Suite 110
Los Altos, CA 94022

Prof. John H. Woodhouse
Hoffman Laboratory
Harvard University
20 Oxford St.
Cambridge, MA 02138

Prof. Francis T. Wu
Department of Geological Sciences
State University of New York
at Binghamton
Vestal, NY 13901

Dr. Gregory B. Young
ENSCO, Inc.
5400 Port Royal Road
Springfield, VA 22151-2388

GOVERNMENT

Dr. Ralph Alewine III
DARPA/NMRO
1400 Wilson Boulevard
Arlington, VA 22209-2308

Mr. James C. Battis
GL/LWH
Hanscom AFB, MA 01731-5000

Dr Robert Blandford
AFTAC/TT
Center for Seismic Studies
1300 No. 17th St, Suite 1450
Arlington, VA 22209

Eric Chael
Division 9241
Sandia Laboratory
Albuquerque, NM 87185

Dr. John J. Cipar
GL/LWH
Hanscom AFB, MA 01731-5000

Cecil Davis
Group P-15, Mail Stop D406
P.O. Box 1663
Los Alamos National Laboratory
Los Alamos, NM 87544

Mr. Jeff Duncan
Office of Congressman Markey
2133 Rayburn House Bldg.
Washington, DC 20515

Dr. Jack Evernden
USGS - Earthquake Studies
345 Middlefield Road
Menlo Park, CA 94025

Art Frankel
USGS
922 National Center
Reston, VA 22092

Dr. Dale Glover
DIA/DT-1B
Washington, DC 20301

Dr. T. Hanks
USGS
Nat'l Earthquake Research Center
345 Middlefield Road
Menlo Park, CA 94025

Dr. James Hannon
Lawrence Livermore Nat'l Laboratory
P.O. Box 808
Livermore, CA 94550

Paul Johnson
ESS-4, Mail Stop J979
Los Alamos National Laboratory
Los Alamos, NM 87545

Janet Johnston
GL/LWH
Hanscom AFB, MA 01731-5000

Dr. Katharine Kadinsky-Cade
GL/LWH
Hanscom AFB, MA 01731-5000

Ms. Ann Kerr
IGPP, A-025
Scripps Institute of Oceanography
University of California, San Diego
La Jolla, CA 92093

Dr. Max Koontz
US Dept of Energy/DP 5
Forrestal Building
1000 Independence Avenue
Washington, DC 20585

Dr. W.H.K. Lee
Office of Earthquakes, Volcanoes,
& Engineering
345 Middlefield Road
Menlo Park, CA 94025

Dr. William Leith
U.S. Geological Survey
Mail Stop 928
Reston, VA 22092

Dr. Richard Lewis
Director, Earthquake Engineering & Geophysics
U.S. Army Corps of Engineers
Box 631
Vicksburg, MS 39180

James F. Lewkowicz
GL/LWH
Hanscom AFB, MA 01731-5000

Mr. Alfred Lieberman
ACDA/VI-OA'State Department Bldg
Room 5726
320 - 21st Street, NW
Washington, DC 20451

Stephen Mangino
GL/LWH
Hanscom AFB, MA 01731-5000

Dr. Robert Masse
Box 25046, Mail Stop 967
Denver Federal Center
Denver, CO 80225

Art McGarr
U.S. Geological Survey, MS-977
345 Middlefield Road
Menlo Park, CA 94025

Richard Morrow
ACDA/VI, Room 5741
320 21st Street N.W
Washington, DC 20451

Dr. Keith K. Nakanishi
Lawrence Livermore National Laboratory
P.O. Box 808, L-205
Livermore, CA 94550

Dr. Carl Newton
Los Alamos National Laboratory
P.O. Box 1663
Mail Stop C335, Group ESS-3
Los Alamos, NM 87545

- Dr. Kenneth H. Olsen
Los Alamos Scientific Laboratory
P.O. Box 1663
- Mail Stop D-406
Los Alamos, NM 87545

Howard J. Patton
Lawrence Livermore National Laboratory
P.O. Box 808, L-205
Livermore, CA 94550

Mr. Chris Paine
Office of Senator Kennedy
SR 315
United States Senate
Washington, DC 20510

Colonel Jerry J. Perrizo
AFOSR/NP, Building 410
Bolling AFB
Washington, DC 20332-6448

Dr. Frank F. Pilotte
HQ AFTAC/TT
Patrick AFB, FL 32925-6001

Katie Poley
CIA-OSWR/NED
Washington, DC 20505

Mr. Jack Rachlin
U.S. Geological Survey
Geology, Rm 3 C136
Mail Stop 928 National Center
Reston, VA 22092

Dr. Robert Reinke
WL/NTESG
Kirtland AFB, NM 87117-6008

Dr. Byron Ristvet
HQ DNA, Nevada Operations Office
Attn: NVCG
P.O. Box 98539
Las Vegas, NV 89193

Dr. George Rothe
HQ AFTAC/TTR
Patrick AFB, FL 32925-6001

Dr. Alan S. Ryall, Jr.
DARPA/NMRO
1400 Wilson Boulevard
Arlington, VA 22209-2308

Dr. Michael Shore
Defense Nuclear Agency/SPSS
6801 Telegraph Road
Alexandria, VA 22310

Dr. Albert Smith
Los Alamos National Laboratory
L-205
P. O. Box 808
Livermore, CA 94550

Donald L. Springer
Lawrence Livermore National Laboratory
L-205
P. O. Box 808
Livermore, CA 94550

Mr. Charles L. Taylor
GL/LWG
Hanscom AFB, MA 01731-5000

Dr. Steven R. Taylor
Lawrence Livermore National Laboratory
L-205
P. O. Box 808
Livermore, CA 94550

Dr. Larry Turnbull
CIA-OSWR/NED
Washington, DC 20505

Dr. Eileen Vergi o
Lawrence Livermore National Laboratory
L-205
P. O. Box 808
Livermore, CA 94550

Dr. Thomas Weaver
Los Alamos National Laboratory
P.O. Box 1663, Mail Stop C335
Los Alamos, NM 87545

J.J. Zucca
Lawrence Livermore National Laboratory
P. O. Box 808
Livermore, CA 94550

GL/SULL
Research Library
Hanscom AFB, MA 01731-5000 (2 copies)

Secretary of the Air Force
(SAFRD)
Washington, DC 20330

Office of the Secretary Defense
DDR & E
Washington, DC 20330

HQ DNA
Attn: Technical Library
Washington, DC 20305

DARPA/RMO/RETRIEVAL
1400 Wilson Boulevard
Arlington, VA 22209

DARPA/RMO/Security Office
1400 Wilson Boulevard
Arlington, VA 22209

Geophysics Laboratory
Attn: XO
Hanscom AFB, MA 01731-5000

Geophysics Laboratory
Attn: LW
Hanscom AFB, MA 01731-5000

DARPA/PM
1400 Wilson Boulevard
Arlington, VA 22209

Defense Technical Information Center
Cameron Station
Alexandria, VA 22314 (2 copies)

Defense Intelligence Agency
Directorate for Scientific
& Technical Intelligence Attn: DT1B
Washington, DC 20340-6158

AFTAC/CA
(STINFO)
Patrick AFB, FL 32925-6001

TACTEC - Battelle Memorial Institute
505 King Ave.
Columbus, OH 43201 (FINAL REPORT ONLY)

CONTRACTORS (Foreign)

Dr. Ramon Cabre, S.J.
Observatorio San Calixto
Casilla 5939
La Paz, Bolivia

Prof. Hans-Peter Harjes
• Institute for Geophysik
Ruhr University/Bochum
P.O. Box 102148
• 4630 Bochum 1, FRG

Prof. Eystein Husebye
NTNF/NORSAR
P.O. Box 51
N-2007 Kjeller, NORWAY

Prof. Brian L.N. Kennett
Research School of Earth Sciences
Institute of Advanced Studies
G.P.O. Box 4
Canberra 2601, AUSTRALIA

Dr. Bernard Massinon
Societe Radiomana
27 rue Claude Bernard
75005 Paris, FRANCE (2 Copies)

Dr. Pierre Mecheler
Societe Radiomana
27 rue Claude Bernard
75005 Paris, FRANCE

Dr. Svein Mykkeltveit
NTNF/NORSAR
P.O. Box 51
N-2007 Kjeller, NORWAY

FOREIGN (Others)

Dr. Peter Basham
Earth Physics Branch
Geological Survey of Canada
1 Observatory Crescent
Ottawa, Ontario, CANADA K1A 0Y3

Dr. Eduard Berg
Institute of Geophysics
University of Hawaii
Honolulu, HI 96822

Dr. Michel Bouchon
I.R.I.G.M.-B.P. 68
38402 St. Martin D'Heres
Cedex, FRANCE

Dr. Hilmar Bungum
NTNF/NORSAR
P.O. Box 51
N-2007 Kjeller, NORWAY

Dr. Michel Campillo
Observatoire de Grenoble
I.R.I.G.M.-B.P. 53
38041 Grenoble, FRANCE

Dr. Kin Yip Chun
Geophysics Division
Physics Department
University of Toronto
Ontario, CANADA M5S 1A7

Dr. Alan Douglas
Ministry of Defense
Blacknest, Brimpton
Reading RG7-4RS, UNITED KINGDOM

Dr. Roger Hansen
NTNF/NORSAR
P.O. Box 51
N-2007 Kjeller, NORWAY

Dr. Manfred Henger
Federal Institute for Geosciences & Nat'l Res.
Postfach 510153
D-3000 Hannover 51, FRG

Ms. Eva Johannisson
Senior Research Officer
National Defense Research Inst.
P.O. Box 27322
S-102 54 Stockholm, SWEDEN

Dr. Fekadu Kebede
Seismological Section
Box 12019
S-750 Uppsala, SWEDEN

Dr. Tormod Kvaerna
NTNF/NORSAR
P.O. Box 51
N-2007 Kjeller, NORWAY

Dr. Peter Marshal
Procurement Executive
Ministry of Defense
Blacknest, Brimpton
Reading RG7-4RS, UNITED KINGDOM

Prof. Ari Ben-Menahem
Department of Applied Mathematics
Weizman Institute of Science
Rehovot, ISRAEL 951729

Dr. Robert North
Geophysics Division
Geological Survey of Canada
1 Observatory Crescent
Ottawa, Ontario, CANADA K1A 0Y3

Dr. Frode Ringdal
NTNF/NORSAR
P.O. Box 51
N-2007 Kjeller, NORWAY

Dr. Jorg Schlittenhardt
Federal Institute for Geosciences & Nat'l Res.
Postfach 510153
D-3000 Hannover 51, FEDERAL REPUBLIC OF
GERMANY